Constraints on Neptune's haze structure and formation from VLT observations in the H-band

Daniel Toledo [a], Patrick G. J. Irwin [a], Pascal Rannou [b], Leigh N. Fletcher [c], Nicholas A. Teanby [d], Michael H. Wong [e], and Glenn S. Orton [f]

[a] *Atmospheric, Oceanic and Planetary Physics, University of Oxford, UK*

[b] *GSMA, Universite de Reims Champagne-Ardenne, UMR 7331-GSMA, 51687 Reims, France*

[c] *Department of Physics & Astronomy, University of Leicester, Leicester, UK*

[d] *School of Earth Sciences, University of Bristol, Wills Memorial Building, Queens Road, Bristol, BS8 1RJ, UK*

[e] *University of California at Berkeley Astronomy Department Berkeley, CA 947200-3411, USA*

[f] *Jet Propulsion Laboratory, California Institute of Technology, 4800 Oak Grove Drive, Pasadena, CA 91109, USA*

Number of pages: 34

Number of tables: 1

Number of figures: 23

Proposed Running Head:

Constraints on Neptune's haze structure and formation from VLT observations in the H-band

Please send Editorial Correspondence to:

Daniel Toledo Carrasco

University of Oxford

Clarendon laboratory

Parks road, Oxford, OX1 3PU, UK.

Email: daniel.toledocarrasco@physics.ox.ac.uk

ABSTRACT

A 1-dimensional microphysics model has been used to constrain the structure and formation of haze in Neptune's atmosphere. These simulations were coupled to a radiative-transfer and retrieval code (NEMESIS) to model spectral observations of Neptune in the H-band performed by the SINFONI Integral Field Unit Spectrometer on the Very Large Telescope (VLT) in 2013. It was found that observations in the H-band and with emission angles $\leq 60^{\circ}$ are largely unaffected by the imaginary refractive index of haze particles, allowing a notable reduction of the free parameters required to fit the observations. Our analysis shows a total haze production rate of $(2.61\pm0.18)\times10^{-14}$ kg m^{-2} s^{-1}, about 10 times larger than that found in Uranus's atmosphere, and a particle electric charge of q=8.6±1.1 electrons per μm radius at latitudes between 5 and 15° S. This haze production rate in Neptune results in haze optical depths about 10 times greater than those in Uranus. The effective radius r_{eff} was found to be 0.22±0.01 and 0.26±0.02 μm at the 0.1 and 1-bar levels, respectively, with haze number densities of $8.48^{-1.31}_{+1.78}$ and $9.31^{-1.91}_{+2.52}$ particles per cm^3. The fit at weak methane-absorbing wavelengths reveals also the presence of a tropospheric cloud with a total optical depth > 10 at 1.46 μm. The tropospheric cloud base altitude was found near the 2.5-bar level, although this estimation may be only representative of the top of a thicker and deeper cloud.

Our analysis leads to haze opacities about 3.5 times larger than that derived from Voyager-2 observations (Moses et al., 1995). This larger opacity indicates a haze production rate 2 times larger at least. To study this difference haze opacity or production rate, we performed a timescale analysis with our microphysical model to estimate the time required for haze particles to grow and

settle out. Although this analysis shows haze timescales ($\sim$15 years) shorter than the time lapsed between Voyager-2 observations and 2013, the solar illumination at the top of the atmosphere has not varied significantly during this period (at the studied latitudes) to explain the increase in haze production. This difference in haze production rate derived for these two periods may arise from: a) the fact that in our analysis we employed spectral observations in the infrared (H-band), while Moses et al. (1995) used photometric images taken at 5 different filters in the visible. While high-phase-angle Voyager observations are more sensitive to small haze particles and at altitudes above the 0.1-bar level, the haze constraints derived from VLT spectra in H-band are limited to pressures greater than 0.1 bar. As a result of the different phase angles of the two set of observations, differences in the estimation of M_0 may arise from the use of Mie phase functions as well. b) our 1-dimensional model does not account for latitudinal redistributions of the haze by dynamics. A possible meridional transport of haze with wind velocities greater than $\sim$0.03 ms^{-1} would result in dynamics timescales shorter than 15 years and thus might explain the observed variations in the haze production rate during this period. Compared with our estimations, photochemical models point to even larger production rates on Neptune (by a factor of 2.4). Assuming that the photochemical simulations are correct, we found that this discrepancy can be explained if haze particles evaporate before reaching the tropospheric-cloud levels. This scenario would decrease the cumulative haze opacity above the 1-bar level, and thus a larger haze production rate would be required to fit our observations. However, to validate this haze vertical structure future microphysical simulations that include the evaporation rates of haze particles are required.

Keywords: Neptune; haze microphysics; radiative transfer;

1 Introduction

Analyses of high-phase-angle Voyager-2 images indicated the presence of hazes in the atmosphere of Neptune (e.g. Smith et al., 1989). As in Uranus's atmosphere, the haze formation is attributed to the condensation of hydrocarbons such as C_2H_6 or C_2H_2 in the stratosphere ~ 0.016 mbar. These hydrocarbons are the product of methane dissociation by solar UV and energetic particles that leads to a number of chemical reactions (Moses et al., 1995, 2018). The condensation of the hydrocarbons into their respective ices results in the formation of the initial haze particles at different altitudes. These initial haze particles, which cannot be detected from ground-based observations due to their small size (radii < 0.1 μm), can grow in size very quickly by particle coagulation, and then sink deeper into the atmosphere. Estimations of the haze vertical structure (size distribution and density) can be performed using radiative-transfer simulations. For instance, analyses of limb observations taken at different tangent heights can provide strong constraints on the vertical haze density or size distribution. However, our current observations, ground-based telescopes or observations from telescopes in orbit around the earth, do not allow us to perform these kind of analyses and usually the radiative-transfer analyses must assume some properties of the haze such as the vertical distribution. A number of radiative-transfer simulations have been performed to study the aerosol properties in Neptune's atmosphere (e.g. Karkoschka and Tomasko, 2011; Irwin et al., 2014, 2016a). Although all these analyses required hazes in their respective models to fit the observations, the haze structure (number density and size distribution) used or estimated by their analyses were very different. While Irwin et al. (2016a) analyzed VLT spectra in the H-

band (1.4-1.8 μm) using a 2-cloud model compromising a vertically extended haze layer and a tropospheric compact cloud, Karkoschka and Tomasko (2011) used a model with different haze layers between the 10 and 0.01-bar levels without compact clouds to analyse data cube of Neptune acquired with the Hubble STIS spectrograph. Based on the χ^2 analysis, both models were found to provide good fits to the respective observations despite the different haze structure of the models. These different radiative-transfer analyses show the limitations of determining precisely the scattering and vertical distribution properties of the haze from remote observations alone.

Some previous analyses used haze microphysics simulations to provide constraints on the density and size distribution of the haze vertical profiles. For Uranus's haze, Toledo et al. (2019) combined a microphysical model (Cabane et al., 1992; Rannou et al., 2004) with the NEMESIS radiative-transfer code (Irwin et al., 2008) to analyse VLT observations in the H-band. For Neptune's haze, Moses et al. (1995) analyzed high-phase-angle Voyager-2 images combining models of haze microphysics (Toon et al., 1980) and photochemistry (Moses et al., 1992) to constrain the haze formation and structure. Although this analysis provided strong constraints on haze properties, a number of observations have revealed seasonal changes in Neptune's brightness after the Voyager-2 observations (e.g. Lockwood and Thompson, 2002; Aplin and Harrison, 2016). These changes in brightness, which are associated with changes in the albedo from hazes and clouds, point out the need of performing new haze microphysics simulations of the formation and growth of haze in Neptune's atmosphere. In this work we analysed observations acquired in 2013 using the SINFONI Integral Field Unit Spectrometer on the VLT in the H-band with a microphysical code following the approach of Toledo et al. (2019). In order to fit the spectral observations, the haze microphysical simulations were coupled

with NEMESIS. We describe the data utilized in this work, the microphysical model, and radiative-transfer codes in section 2. In sections 3, 4 and 5 we present our model results, compare them to data, and discuss the impact of dynamics on the distribution of the haze in Neptune's atmosphere.

2 Observations, haze microphysics and radiative transfer

2.1 Observations

We analyzed observations of Neptune in the H-band (1.4-1.8 μm) performed by the SINFONI instrument in October 2013 (Irwin et al., 2016a), at the European Southern Observatory (ESO) VLT in Paranal, Chile. These observations were performed with a spatial resolution of about 0.1", returning 64×64-spatial-pixel spectral cubes with a spectral resolution of 0.0005 μm. Data reduction was carried out with the ESO VLT SINFONI pipeline and additional photometric corrections as described in by Irwin et al. (2016b) were also included. The reduced data were then averaged with a triangular-shaped instrument function with full width half maximum = 0.002 μm, resulting in a final spectral resolution of R$\sim$775. It was found in previous analyses of Neptune that this spectral resolution provides the best compromise between modeling computational speed, signal-to-noise ratio, and accurate representation of the methane absorption features (Irwin et al., 2014, 2016a).

2.2 Haze microphysics and radiative transfer

The same 1-dimensional haze microphysics model used in Toledo et al. (2019) for Uranus was employed in this study to simulate the formation and evolution of haze in Neptune. This 1-dimensional Eulerian model, first used to study the haze in Titan's atmosphere (Cabane et al., 1992; Rannou et al., 2004), solves the aerosol continuity equation to simulate the time evolution of a given population of particles, described in terms of particle radius and altitude, whose production occurs in the stratosphere. The different processes involved in the time variation of the population of particles are the particle coagulation, settling and eddy diffusion. The production rate of particles Q at a given altitude z is parametrized by a sum of Gaussian functions

$$Q(z) = \sum_{i=1}^{n} Q_i exp\left(-\frac{(z - z_{0i})^2}{2\Delta z_i^2}\right) \quad (1)$$

where n represents the number of condensable species (i.e. C_2H_6, C_2H_2) whose vertical production region is parametrized by the adjustable parameters z_{0i} (altitude of maximum of production) and Δz_i (extension of the haze-production region). For each condensable species, the term Q_i is given by

$$Q_i = \frac{M_{0i}}{(4/3)\pi\rho_i r_0^3} \frac{1}{\sqrt{2\pi}\Delta z_i} \quad (2)$$

where M_{0i} is the vertically-integrated production rate (kg m^{-2} s^{-1}) of species i, r_0 is the initial model particle radius (set to 0.0012 μm) and ρ_i is the density of the material making up the particles (fixed to 700 kg m^{-3}). The parameter M_{0i} determines the mass of haze produced by the condensation of species i

in the stratosphere and its range of values is estimated in our simulations. In our analysis we have assumed a single condensible species (n=1) with z_0 set to the altitude corresponding to the ∼0.016-bar level (Moses et al., 1995) and Δz to 2.5 km. In section 3.4 we will discuss the impact of adding multiple condensation rates on the haze retrievals. For modelling the coagulation rate in a given radius bin, we need to specify the sticking coefficient (s) that represents the probability that two particles will stick together (Pollack et al., 1987). The value of s for two particles of radius r_1 and r_2 is given by

$$s = exp\left(\frac{-q^2 r_1 r_2}{kT(r_1 + r_2)}\right) \tag{3}$$

where T is the temperature, k is the Boltzmann's constant and q is the haze charge-per-unit-radius parameter (expressed in electrons per micrometre of radius) which, together with M_0, is estimated in our simulations. The last parameter required for the model is the eddy diffusion coefficient (K) whose profile for Neptune's atmosphere is illustrated in Figure 1. The eddy diffusion was computed by

$$K(p) = K_0\left(\frac{p}{kT}\right)^{-0.5} \tag{4}$$

where the constant K_0 was estimated from K at a given reference pressure level. The temperature profile used in equation 4, displayed in Fig. 1, is based on the 'N' profile estimated by radio-occultation from Voyager 2 by Lindal (1992) with an He:H_2 ratio of 0.177. This He:H_2 ratio results in a helium volume mixing ratio of 0.15 at altitudes of negligible methane abundance (assuming 0.3% nitrogen). For a set of values of M_0 and q the code computes the vertical haze profiles of number density and size distribution. Since we are using a 1-dimensional model, latitudinal variations of K and T are not

accounted in the simulations. However, in sections 3.3 and 3.5 we will discuss how variations in the K and T profiles may affect our haze properties estimations.

For simulations of the scattering and absorption of gases and aerosols in Neptune's atmosphere, the NEMESIS correlated-k radiative transfer and retrieval code (Irwin et al., 2008) was used. The scattering properties of aerosols were computed using Mie theory with phase functions approximated at each wavelength with combined Henyey-Greenstein functions to average over the characteristic "glory" and "rainbow" of pure spherical particles. The same atmospheric model as described in Irwin et al. (2014, 2016a) was used to model the spectra. The methane abundance profile was set with a deep CH4 mole fraction of 4% and the volume mixing ratio limited to a maximum relative humidity of 60%, as recommended by Karkoschka and Tomasko (2011), but the stratospheric abundance was set to $(1.5 \pm 0.2) \times 10^{-3}$ as recommended by Lellouch et al. (2010).The methane absorption in the H-band was computed using the 'WKMC-80K' line database (Campargue et al., 2012). The methane line data were converted to k-distribution look-up tables covering the spectral range of the VLT observations and assuming a triangular-shaped instrument function with full width half maximum=0.002 μm. Collision-induced absorption by H_2–H_2 and H_2–He were computed using the coefficients of Borysow et al. (1989), Borysow et al. (2000), and Zheng and Borysow (1995), and an equilibrium ortho/para-H_2 was assumed at all altitudes and locations. Absorption by H_2–CH_4 and CH_4–CH_4 collision-induced was also computed (Borysow and Frommhold, 1987).

3 Retrieval analysis

3.1 H-band observations

To estimate the haze parameters M_0 and q in Neptune's atmosphere, we used the haze microphysics and NEMESIS radiative-transfer codes as described in Toledo et al. (2019). VLT H-band spectra were fitted with NEMESIS using an aerosol model comprising a tropospheric cloud and a haze layer whose profiles of particle size and number density are computed with the microphysical model for a set of values of M_0 and q. The cross section (σ), phase function ($p(\theta)$) and single-scattering albedo (ω) of aerosol required for the radiative-transfer simulations were computed using Mie theory for a given aerosol refractive index and size distribution. In previous analyses the imaginary refractive index spectrum of the haze and the tropospheric cloud was fitted. In order to analyse the impact of the imaginary refractive index (k) on the observations, simulations of VLT observations in the H-band for different values of k for the haze particles and a constant effective radius of 0.3 μm are shown in Figure 2. These simulations indicate that an increase in k has a little impact on the simulated spectrum. Although at weak methane-absorbing wavelengths (e.g. at 1.585 μm) some variations can be observed, it is important to note here that the haze microphysics parameters are mainly constrained from the observations at strong methane-absorbing wavelengths (1.46, 1.64 and 1.7 μm) since only the high troposphere or stratosphere is sampled. That is to say, the haze microphysics parameters are, in this case, mainly retrieved from the observations for which k does not have a significant effect.

In order to further study the haze scattering properties in the H-band, the

spectrum of ω, σ and the scattering cross-section (σ_S) computed for the k and r_{eff} values used in Fig. 2 are illustrated in Figure 3. This figure indicates that an increase in k results in a smaller ω (Fig. 3a) and a greater σ (Fig. 3b). The light scattered by the haze in a given level depends on both the haze number density and the scattering cross-section, defined as $\sigma_S = \sigma \times \omega$. Fig. 3c shows that in the H-band range, the scattering cross-section is practically the same for k=0.0001, 0.01 and 0.04. This is due to the fact that in the H-band range the increases/decreases in ω with k are compensated by the decreases/increases in σ, resulting in a practically constant $\sigma_S = \sigma \times \omega$. These results explain the negligible impact of the imaginary refractive index on the simulated spectrum shown in Fig. 2. Therefore, these results indicate that for simulating a VLT spectrum in the H-band we can use a constant imaginary refractive index for haze particles and, therefore, reduce the number of free parameters in the model.

3.2 Aerosol model

Similar to previous work (see Irwin et al., 2018), the effective particle radius and vertical distribution of the tropospheric cloud were fitted in our analysis. The vertical cloud number density was characterised by the total opacity (τ_{tc}), the fractional scale height (FSH) and the cloud base altitude (CBA). It is important to note that for haze retrievals we can use a constant imaginary refractive index because the effective radius of particles is smaller than 0.5 μm. However, since the radii of the particles of the tropospheric cloud can achieve values greater than 0.5 μm, the spectrum of the refractive index has an important impact on the simulations. Indeed, it can be demonstrated

that as r_{eff} increases, the differences between the simulated spectra of Fig. 2 become bigger. Therefore, the spectrum of the imaginary refractive index for the tropospheric cloud was retrieved, and the real refractive index at a single wavelength was set to a reference value of 1.4 (see Irwin et al., 2017, 2018); the real part of the refractive index at all other wavelengths was calculated using the Kramers-Kronig relation (see Sheik-Bahae, 2005). The free parameters in our model are, therefore, M_0 and q for the haze, and τ_{tc}, FSH, CBA, the size distribution (r_{eff}, ν_{eff}) and the imaginary refractive index for the tropospheric cloud. Figure 4 shows, as example, the effect of varying the haze production rate M_0 (upper panel) and the tropospheric cloud opacity τ_{tc} (lower panel) on the simulated H-band spectrum. These simulations indicate that the haze production rate has consequences for the whole of the H-band spectrum measured by VLT. However, this is not the case for the tropospheric cloud opacity for which we only observe variations in the simulated spectrum at the weak methane-absorbing wavelengths. These simulations indicate that by fitting only the observations at strong methane-absorbing wavelengths, we can derive the haze properties independently of the tropospheric cloud parameters.

3.3 Haze retrievals

To estimate the haze parameters M_0 and q in Neptune with our model, we chose to analyse VLT observations in regions free of high clouds. Neptune images are displayed in Figure 5, along with the spectra that result from the average of the observations in the pixels indicated in red and blue. These pixels were grouped according to latitude and emission-angle range: the spectrum in

red (see Fig. 5b) was computed from all the pixels at latitudes between 0 and 15° S (note that this region is free of high clouds) and with emission angles of between 20 and 25°, while the spectrum in blue from pixels with emission angles of between 50 and 55° and the same latitude range. To cover a wide range of emission angles in our analysis, we fitted simultaneously a total of 6 spectra computed as those shown in the right panel of Fig. 5 but for the emission-angle ranges [20°-25°], [30°-35°], [40°-45°], [50°-54°], [55°-58°] and [59°-60°]. For these emission-angle ranges we tested the validity of the results shown in the previous section, and found that to fit these observations a constant imaginary refractive index can be used (in this analysis we used a refractive index of n=1.4+0.0001i). However, Irwin et al. (2011, 2016a) found that for limb-darkening analyses including spectra with emission angles greater than 60° the haze imaginary refractive index has an impact on the simulated spectra. Since in this work we are focused on estimating the haze parameters M_0 and q, our limb-darkening analysis comprises only spectra with emission angles $\leq$ 60°, allowing a notable reduction of the free parameters required to fit the observations. Figure 6 shows a comparison between observations (thick red solid lines) and simulations (blue line) performed for M_0=2.5×10^{-14} kg m^{-2} s^{-1} and q=10 electrons per μm radius. Note that because in this section we are only interested in estimating the haze parameters, these simulations are only performed for the observations at strong methane-absorbing wavelengths (in the spectral ranges 1.46-1.6 μm and 1.65-1.71 μm). Therefore, we can simulate the observations illustrated in Fig. 6 to find which range of values of M_0 and q can fit the observations.

In order to speed up the simulations, the retrieval procedure makes use of a pre-computed set of look-up tables of the haze number density and size distribution for a number of combinations of M_0 and q. For each combination of M_0

and q, we fitted simultaneously the 6 spectra shown in Fig. 6 with NEMESIS code at the strong methane-absorbing wavelengths. Figure 7 shows the contour plots of χ^2 in the M_0-q space of the analysis, along with 3σ significance level of χ^2 (red solid line). The analysis provides a χ^2 minimum of 423.97, value that corresponds to a reduced χ^2 (defined as $\chi^2/N_{observations}$) of 0.64. If we define the errors of M_0 and q as the ΔM_0 and Δq that give a $\Delta\chi^2$=11.8 (value corresponding to the 3σ significance level), then our analysis provides a $M_0=(2.61\pm0.18)\times10^{-14}$ kg m^{-2} s^{-1} and a q=8.6$\pm$1.1 electrons per μm radius. For these retrievals the temperature and eddy-diffusion profiles illustrated in Fig. 1 were used to simulate the haze microphysics. However, some latitudinal variations in the values of these parameters could be expected. In order to study how such variations can affect our estimations of the haze parameters, the left panel of Figure 8 shows the pressure levels at which the haze scattering optical depth τ_s are 0.01 and 0.04 for different T profiles. In all of these simulations the only variable that was changed is the temperature profile. These T profiles are defined as $T=\Delta T+T_0$, where T_0 is the temperature profile shown in Fig. 1. These variations in the haze optical depth with T can be compared with those observed when the haze production rate changes (right panel of Fig. 8). We observe that a variation in M_0 of 7% (note that this is the error in our estimation of M_0) produces a variation in the pressure level at which τ_s=0.04 of $\Delta p=\pm\sim0.4$ bar (see right panel of Fig. 8). We note that to produce such a change in the pressure level of τ_s=0.04 the temperature must vary by $\Delta T=\pm\sim6$ K. Therefore, these simulations indicate that latitudinal variations in the temperature are not expected to change notably our estimation of M_0 as long as they are smaller than 6 K. A similar analysis was performed for the eddy-diffusion profile, which simulates the transport of haze particles in the low stratosphere and troposphere. In this case we multiplied K_0 of equation

4 by different factors, from 0.1 up to 10, to study the variation of the haze optical depth with the eddy-diffusion profile. These simulations, illustrated in Figure 9, indicate that the haze optical depth variations with K_0 are smaller than those observed when M_0 varies by a 7%. Therefore, these simulations show that latitudinal variations in the values of T and K are not expected to cause a significant effect on our estimations of the haze parameters.

3.4 Tropospheric cloud retrievals

In our prior analysis the haze retrievals were decoupled from the tropospheric cloud parameters by fitting only the observations at strong methane-absorbing wavelengths. In our current analysis we fitted the whole VLT H-band spectrum shown in Fig. 6 to estimate the tropospheric cloud parameters: τ_{tc}, FSH, CBA, the size distribution (r_{eff}, ν_{eff}) and the imaginary refractive index of cloud particles. For these retrievals the haze parameters were kept constant to the values derived in previous section. This analysis provides the best fit shown in Figure 10 with τ_{tc}=$\sim$ 12 at 1.46 μm, CBA=$\sim$ 2.5 bar. Regarding the size of the particles, presumably made of H_2S ice (Irwin et al., 2018, 2019), we found that particles with r_{eff} in the rage of 2.-2.6 μm provide the best fit between observations and simulations. However, it is important to note here that as a result of its large opacity these retrievals may be only representative of the top of a thicker and deeper tropospheric cloud. In order to compare these retrievals with those given in previous section, Figure 11 shows the vertical profiles of size, number density and scattering cumulative optical depth of both the tropospheric cloud and the haze. For comparison purposes, the haze profiles derived for Uranus (Toledo et al., 2019) are also displayed in Fig.

11. This comparison indicates tropospheric cloud particles on Neptune much bigger in size and number density (for p>0.04 bar), resulting in optical depths of about 250 larger than those due to hazes. Therefore, comparing these results with the haze opacities shown in Fig.8 and Fig. 9, we find that dispersion by cloud particles dominates for altitudes below the cloud top. We also observe that the haze in Neptune is greater in size and number density than the haze in Uranus for p>0.02 bar as a result of the greater haze production rate (M_0 in Neptune is about 10 times bigger). This results from the fact that methane molecules can reach higher altitudes in Neptune than in Uranus because of the higher eddy diffusion coefficient of this planet (Moses et al., 1995). Therefore, this indicates that while the eddy diffusion does not have a major impact on the transport of haze particles in the low stratosphere and troposphere (section 3.3), it does have a major impact on M_0 through the transport of gases in the region of the atmosphere where the methane photolysis takes place (near the 10^{-3}-mbar level). That is to say, greater eddy-diffusion coefficients in the high stratosphere result in a greater haze production rate (parameter estimated in our analysis).

3.5 Haze production analysis

In our previous analysis, we have assumed a simplistic 1-region model for the production of haze. This scheme assumes that species such as C_2H_2 or C_4H_2 condense at the same region of the atmosphere. In order to study the impact of this simplification on the estimation of the haze parameters, we performed microphysics simulations using 3 different models of haze production, whose vertical distribution is characterized by equation 1. The values of p_{0i} and M_{0i}

used for each of these models are given in Table 1. Note that while model-1 corresponds to our 1-region model used in the previous sections, model-2 and model-3 compromise 3 different vertical regions of haze production. The pressure level p_{0i} and value of M_{0i} for each region were chosen according to Moses et al. (1995). Note that the total haze production M_0 is the same for the 3 models. The profiles of haze number density and optical depth obtained for these different models are displayed in Figure 12. The different haze production regions of model-2 and model-3 can be identified through the maxima of number density above the 0.1-bar level. Although some variations in the density profiles can be observed above the 0.03-bar level, the density profiles below this pressure level converge toward the same solution. To test whether this different vertical structure above the 0.03-bar level can be significant in our observations we need to study the cumulative optical depth. In the previous section we have mentioned that our observations are not sensitive to variations in the aerosol optical depth smaller than 5.10^{-4}. By studying the optical depth profiles given in the lower panel of Fig. 12, we observe that the largest variations in optical depth are given for model-1 and model-2. However, these differences, only observed for altitudes above the 0.04-bar level, are in any case smaller than 5.10^{-4}. These results show, therefore, that even the simplistic 1-region model provides similar results than those given by the 3-region models.

Following this study of the impact of using a 1-region model for the production of haze, the next step in this analysis is to test the importance of the radius of the initial haze particles. In all our models of haze production, we have assumed an initial model radius of 0.0012 μm. Since our estimations of haze production rate are given in units of mass, this means that for a bigger initial model radius the number of initial haze particles must be smaller to

keep constant M_0. The number of haze particles produced in a given region of the atmosphere depends on the population of nuclei (assuming heterogeneous nucleation) and the concentration of condensable species. However, the number concentration of this population of nuclei, as well as its nature, is poorly constrained, which directly implies the need to assume a value of r_0. Different initial radii may lead to different time rates of coagulation and, hence, to different haze profiles. As we will discuss in next section, the particle coagulation depends on the concentration of particles and the collection kernel K_c, whose value for particles of radii r_i and r_j is computed assuming classical assumptions (Fuchs, 1964; Cabane et al., 1992):

$$K_c(r_i, r_j) = 4\pi(D_i + D_j)(r_i + r_j)\beta \tag{5}$$

where D is the diffusion coefficient and β is a correction factor whose value is $\approx$1 for Kn(Knudsen number)$\ll$1 or $\beta \approx V_{ij}(r_i + r_j)s/[4(D_i + D_j)]$ for Kn$\gg$1, where V_{ij} is the the mean thermal velocity. Figure 13 shows the variation of K_c with particle radius at 3 different pressure levels of the haze production region. These K_c are normalized to the value of K_c for r=0.0012 μm. We observe similar values of K_c for radii between 0.0012 and 0.08 μm, and a sharp decrease in K_c for r$>\sim$0.08 μm. Figure 14 illustrates the results of our study of the variation of the haze profiles with r_0 by showing the number density and optical depth computed for a haze production rate of 2.5×10^{-14} kg m^{-2} s^{-1} and different values of r_0. In these simulations we can observe that the initial radius only has a significant effect on the haze concentration in the haze production region. At greater pressures, where the particles are bigger in size, the concentrations obtained using these different initial radii are very similar. This results from the fact that for these initial radii, the values of K_c are very large and similar, leading to very small timescales of

coagulation (practically the same); particles grow up in size very quickly in the 3 cases. In these cases the variation in the estimated haze production rate varies in about a 5 %. Similar simulations as those shown in Fig. 14 indicate that for initial radius greater than 0.05 μm, the variations in the haze profiles can be significant with variations in the haze optical depth $>$ 25 %. However, this upper limit of r_0 represents a extreme case. Therefore, although our model can be simplistic in simulating the vertical region where the haze particles are initially formed, these tests indicate that our estimations are not notably affected by the assumed initial radius or by variations in the altitudes of maximum of production (variations that can be due to changes in the temperature).

4 Comparisons with previous works

4.1 Voyager-2 observations

Our estimated haze production rate leads to an opacity of about 3.5 times larger than that derived in Moses et al. (1995) from Voyager-2 observations (1989). This is shown in Figure 15, that compares haze opacity profiles (at two different wavelengths) computed for: a) the haze parameters given in Moses et al. (1995), M_0=1$\times 10^{-14}$ kg m^{-2} s^{-1} and q=13 electrons per μm (values referred hereafter as M1995 haze parameters); b) the parameters derived in our analysis (referred hereafter as T2020 haze parameters). For comparison purposes, the optical depth for M_0=6$\times 10^{-14}$ kg m^{-2} s^{-1} and q=8.6 electrons per μm is also shown. It is important to note that Moses et al. (1995) used a real refractive index (m) of 1.44 and a density of haze particles ρ_i=1000 kg

m^{-3} (also referred hereafter as M1995 haze parameters), while in this work these parameters were set to m=1.4 and ρ_i=700 kg m^{-3} (e.g. Karkoschka and Tomasko, 2009; Irwin et al., 2016b; Pollack et al., 1987). In order to study the impact of these different opacities on Neptune's spectra, Figure 16 shows comparisons between VLT observations (at strong methane-absorbing wavelengths) and simulations when the two sets of parameters are employed. These results indicate that a reasonably good fit cannot be achieved with VLT spectra and M1995 haze parameters (reduced $\chi^2 \sim 10$). Indeed, the haze opacity obtained for M1995 parameters is too low to reproduce the reflectance spectrum in H-band, and thus it is significantly smaller than our estimations. Next step in our analysis is to evaluate these results in terms of M_0, whose estimation through the haze opacity requires some assumptions. First among them is the real refractive index m whose value, for given profiles of number density and size distribution, mainly determines the haze opacity. Left panel of Figure 17 shows the variation of the haze opacity when m is increased, and the rest of parameters are fixed to T2020 values. For a given M_0, an increase in m results in greater opacities. Thus, the larger is the assumed real refractive index, the smaller the retrieved haze production rate. We examined the impact of using a real refractive index m=1.44, and found that the best fit is achieved for a haze production rate of $\sim 2{\times}10^{-14}$ kg m^{-2} s^{-1}, about 25 % smaller than that obtained for m=1.4. Another parameter whose value has a significant impact on the retrieval of M_0 is the density of the haze particles ρ_i. For a given M_0, a greater ρ_i results in a fewer number of haze particles created per second, and thus a lower opacity (note that the units of M_0 are kg m^{-2} s^{-1}). Right panel of Fig. 17 shows the variation of the haze opacity when ρ_i is increased and the rest of parameters are fixed to T2020 values. In this case, the larger is the assumed ρ_i value, the smaller the number of particles produced

per second, and the larger is the M_0 needed to fit VLT observations. We found that for ρ_i=850 and 1000 kg m^{-3}, the latest the one utilized in Moses et al. (1995), the best fits are obtained for $M_0 = \sim 3.5\times10^{-14}$ and 4.5×10^{-14} kg m^{-2} s^{-1}, respectively. For the rest of model parameters whose values are required (such as the initial model particle radius or the eddy diffusion coefficient), from the results shown in section 3.5 and this section we find that their impact on the estimation of M_0 is negligible compared to that of m or ρ_i. Therefore, based on these results we conclude that our analysis provides a haze production rate significantly greater, at least by a factor of $\sim$ 2, than that derived in Moses et al. (1995).

4.2 Photochemical models

In our analysis, a haze production rate of 2.6×10^{-14} kg m^{-2} s^{-1} was derived for Neptune, about 2.4 times smaller than the $\sim 6\times10^{-14}$ kg m^{-2} s^{-1} value predicted by the photochemical models (Moses et al., 1995), or about 2.5 times larger than that derived from Voyager observations. Figure 18a illustrates a comparison between VLT spectra and simulations performed for a production rate M_0=6×10^{-14} kg m^{-2} s^{-1} and the rest of haze parameters set to T2020 values. These results indicate that this haze production rate leads to opacities not consistent with VLT observations (haze opacity profile illustrated in Fig. 15). Note that a reduced χ^2 of $\sim$ 40 is achieved. In previous section, we showed the impact of m and ρ_i on the haze opacity for a given M_0 (see Fig. 17). Hence, we varied the values of these parameters to study if a better fit can be achieved. Fig. 18b shows, as example, a comparison similar to that in 18a but for a greater ρ_i. Although χ^2 remains large, we can see a noticeable improve-

ment in the fit (reduced $\chi^2 \sim 4$). As similar improvements can be achieved by decreasing m (see Fig. 17), we performed a number of fits similar to those shown in Fig. 18 but for different combinations of these two parameters. Figure 19 illustrates the contour plots of χ^2 in the ρ_i-m space of the analysis, along with 3σ significance level of χ^2 (red solid lines). Note that for this analysis the haze production rate is fixed to M_0=6×10^{-14} kg m^{-2} s^{-1}. The contours of χ^2 indicate two minima with m values of 1.3 and 1.35, and densities of 840 and 1000 kg m^{-3}, respectively. In these cases, the reduced χ^2 values obtained are smaller than 1. Thus, good fits between simulations and VLT observations are achieved using these m and ρ_i values, and the haze production rate predicted by the photochemical models. Although it is difficult to place firm constrains on the density of haze particles, the m values estimated in this analysis can be compared with the real refractive index of the hydrocarbon ices expected to form in Neptune's stratosphere. Photochemical simulations indicate that ethane clearly dominates the haze production rate of the methane photolysis products (Moses et al., 1995, 2018). Hence, we expect haze particles to have a real refractive index m=$\sim$ 1.4, which is characteristic of ethane ice particles. Since the real refractive index values estimated in the analysis of Fig. 19 are significantly smaller, we conclude that these solutions are not consistent with the photochemical simulations.

For the haze profiles computed for M_0=6×10^{-14} kg m^{-2} s^{-1}, we also investigated the impact of setting the haze number density to 0 at altitudes below a certain level in the troposphere (referred thereafter as haze-base pressure p_{haze}). If haze particles are formed by the condensation of hydrocarbons such as ethane, then these particles should partially or totally evaporate in the regions of the atmosphere for which the saturation ratio falls below 1. That is to say, they may begin to evaporate before the fall to the tropospheric-

cloud level. Left panel of Figure 20 shows haze opacity profiles computed for M_0=6×10^{-14} kg m^{-2} s^{-1} and with the haze-base pressure established at 0.36, 0.67 and 1 bar. Note that the haze opacity at pressures greater than p_{haze} is equal to 0. We performed a number of fits similar to that shown in Fig. 18a but setting the haze-base pressure at different levels. The χ^2 variation of these fits with p_{haze} is illustrated in the right panel of Fig. 20. We can see that reasonably good fits are achieved for $p_{haze} \sim 0.55$ bar (reduced $\chi^2 \sim 1.1$). This requires that haze particles should completely evaporate below this pressure level. Abundances of ethane in the troposphere indicate saturations below 1 at altitudes below the $\sim$ 0.3-bar level (Moses et al., 1992). Hence, we conclude that the scenario of haze particles completely evaporated before reaching the levels above tropospheric clouds is plausible. This would result in a significant decrease in the haze opacity with pressure in the subsaturated region, and thus explain the discrepancies found in the estimation of M_0. However, to validate this hypothesis future microphysical simulations that include the evaporation rates of haze particles are required.

5 Timescale analysis and comparisons with Uranus

Once the haze properties were retrieved, our next step is to determine how temporal variations in the haze production rate (due to variations in the solar illumination at the top of the atmosphere) can affect the structure (number density and size distribution) of the haze. To this end, we performed, as in Toledo et al. (2019), a haze microphysics timescale analysis. We first set M_0 and q to the values estimated in section 3.2, and then we run the model, started at time t=0 with no haze in the atmosphere, until the steady state is

achieved (usually for t>140 years). At this moment the haze particle size and density at a given altitude do not change with time. The haze microphysics timescale, defined as t_M, at a given altitude of the atmosphere is given by the time required to achieve the steady state at that altitude. The left panel of Figure 21 shows the haze number density obtained for t=10, 25, 50 and 180 years. Note that the profile obtained for t=180 years represents the steady state of these simulations. Comparing the density profiles for t=10 and 180 years, we observe that the 10-years profile converges towards the steady-state profile for altitudes above the 0.03-bar pressure level. At this altitude, any change in the haze production rate would result in variations in the haze properties 10 years after such a change. Proceeding in the same way for the rest of profiles, we can compute the haze timescale t_M curve as a function of pressure. These results, along with the timescale of Uranus's haze derived in Toledo et al. (2019), are displayed in the central panel of Fig. 21. These simulations indicate that: a) to observe changes in the haze structure (due to changes in the haze production rate) at the 0.1-bar and 1-bar levels, a time lapse of 20 and 70 years must occur, respectively; b) at a given altitude, the haze microphysics timescale in Neptune is shorter than that in Uranus, and the difference in time between both rates (Δt_M=t_M(Neptune)-t_M(Uranus)) increases with pressure. For instance, while at the 0.01-bar level Δt_M is $\sim$10 years, at altitudes below the 0.1-bar level Δt_M is greater than 50 years.

These differences in the haze timescales of both planets arise from the different time rates of the processes involved in the continuity equation: coagulation, settling and eddy diffusion. In left panel of Fig. 11 it has been shown that haze particles in Neptune are greater in size than those in Uranus as a result of the larger haze production rate. These differences in size lead to different haze settling-velocities. This can be observed in the right panel of Fig. 21 that shows

the haze settling-velocities in both planets for the sizes given in left panel of Fig. 11. From the maximum of number density, these results indicate similar settling velocities up to the 0.02-bar level, where the differences in size of haze particles of both planets become more significant (see left panel of Fig. 11). From these velocities we can compute the timescale for sedimentation, t_{fall}, that is defined as the time required for haze particles to fall a distance H:

$$t_{fall} = \frac{H}{v_{fall}} \tag{6}$$

The velocities v_{fall} as a function of pressure are given in Fig. 21c and the distance H is the pressure scale height (H=29 km for Neptune and H=30 km for Uranus). The timescales for sedimentation computed from equation 6 are illustrated in Figure 22a. These results indicate: a) t_{fall} is very similar in both planets for altitudes above the 0.02-bar level; b) t_{fall} in Neptune is smaller than t_{fall} in Uranus for p>0.02 bar; c) the difference between t_{fall} in Neptune and Uranus increases with pressure. By comparing the haze timescales displayed in the central panel of Fig. 21 with the t_{fall} rates given in Figure 22a, we can observe, for pressures greater than 0.03 bar, the high correlation between the differences in t_{fall} of both planets and the differences in the haze timescales Δt_M discussed above.

Although the vertical profiles of v_{fall} can explain the increase of Δt_M with pressure, it is important to note that above the 0.03-bar level any $\Delta t_M > 0$ cannot be explained by t_{fall} since the value of this time rate above that level is very similar in both planets. The density profiles displayed in central panel of Fig. 11 show that the 0.03-bar level corresponds closely to the lower boundary of the haze production region, where the particles grow in size very quickly due to coagulation. It is reasonable to believe, therefore, that above the 0.03-bar level, the differences in the haze microphysics timescales of both planets

are mainly due to the different time rates of coagulation. The timescale of coagulation, t_{coag}, is defined as the time required to reduce the haze number density by 50 %. This time rate depends on the collection kernel K_c, calculated for spherical particles using classical assumptions (Fuchs, 1964), and the haze number density. To estimate t_{coag} we started with the haze given by the steady profiles, and then we run our haze microphysics model up to the time for which the haze concentration has been reduced to 50 % at all the altitudes. For a given altitude, t_{coag} is the exact time at which the density is reduced by 50 %. In order to ensure that any changes in the haze number density are only due to coagulation, these simulations are performed with the haze production rate, the eddy-diffusion profile and the settling velocities set to M_0=0, K=0 and v_{fall}=0. Fig. 22b shows the coagulation timescales for Neptune and Uranus as a function of pressure. Note that because both the number density and K_c changes with pressure, t_{coag} varies with altitude; at higher altitudes where the number density is large and the haze radii small t_{coag} takes smaller values and, hence, it is at these altitude where coagulation dominates the temporal variations of the haze concentration C(r,z). We also observe that t_{coag} is about 10 times smaller in Neptune than in Uranus at the altitudes where the haze is produced as a result of its bigger haze concentration (M_0(Neptune)$\sim$10$\times M_0$(Uranus)). Therefore, these results show that above the 0.03-bar level the haze timescale t_M is dominated by the particle coagulation, and this time constant is smaller in Neptune as a result of its bigger haze production rate (about 10 times).

The last process involved in the continuity equation, and therefore in the time variation of C(r,z), is the eddy diffusion. The time rate of eddy diffusion, defined as t_{diff}, represents the time required for haze particles to be mixed over

a distance H and it is given by

$$t_{diff} = \frac{H^2}{K} \tag{7}$$

where H is the pressure scale height and K is the eddy diffusion coefficient given in Fig. 1. The timescales of eddy diffusion computed from equation 7 are displayed in 22c. These results indicate that as a result of the bigger eddy-diffusion coefficient, the eddy mixing in Neptune's atmosphere is about 10 times more efficient (in terms of t_{diff}) than that in Uranus's. For a given altitude, however, the importance of the eddy diffusion coefficient to the temporal variation of C(r,z) is determined by the values of the time rates t_{diff}, t_{coag} and t_{fall}. For instance, if we find that $t_{diff} \gg t_{coag}$ and t_{fall}, then the eddy mixing does not have a major impact on vertical structure of the haze. In order to study the 3 processes simultaneously, Fig. 22d compares the time rates of t_{diff}, t_{coag} and t_{fall} in Neptune's atmosphere. This comparison indicates that for p<0.04 bar (haze production region), t_{coag} is much smaller than t_{fall} and t_{diff}. At these altitudes the haze number density of particles with r$\sim$r$_0$ is limited by coagulation after $\sim$1 day of being produced. For these radii the particles remain at the same altitude and undergo changes mainly due to particle coagulation ($t_{coag} \ll t_{fall}, t_{diff}$). As the haze particles grow in size, particle removal due to sedimentation takes place, limiting the number of particles of a given size. We can observe that the altitude for which $t_{fall}=t_{coag}$ is at the 0.04-bar level. This level establishes the altitude at which particles with radii of $\sim$0.2 μm are transported by sedimentation a distance H in about the time it takes for coagulation to reduce the concentration in about 50 %. Therefore, at altitudes below the 0.04-bar level, it is the settling velocities v_{fall} that mainly control the time variation of C(r,z). As in Uranus' atmosphere (Toledo et al., 2019), the timescale of eddy diffusion was found to be much bigger than t_{fall}

and t_{coag} at all the altitudes, indicating the little impact of this parameter on the time variation of C(r,z). We also tested the effect that would result from an increase in the eddy diffusion near the tropopause (instead of the decrease illustrated in Fig 1), and we found that our results would not change as long as K values are smaller than $\sim$ 10000 cm^2 s^{-1}.

Our timescale analysis shows that the timescales for aerosols to grow and fall are of about 15 and 30 years at the observable pressure levels in the atmospheres of Neptune and Uranus, respectively. The timescale analysis reveals that the time lapsed between both observations is long enough to observe changes in the haze structure due to microphysics. However, this time lapse represents only a 1/7 of a Neptunian year and for which the solar insolation has not changed significantly at the studied latitudes. Therefore, a significant increase of the haze production rate is not expected, due to variations in the solar insolation at the top of the atmosphere. The different values of M_0 estimated in Moses et al. (1995) and this work may arise from the different kind of data used to constrain the haze parameters. While Moses et al. (1995) analyzed photometric images taken at 5 different filters in the visible, in the present work observations in the infrared were used. As demonstrated in section 3.1, the choice of using observations in the H-band is based on the fact that the observations are practically independent of the haze imaginary refractive index for the emission-angle ranges analysed in section 3.2, allowing a notable reduction of the number of free parameters. However, this different spectral range used to constrain the haze properties may lead to different estimations of M_0 (visible observations are more sensitive to small particles). These discrepancies between both analyses can be studied in future works by applying our model to visible observations or comparing our estimations of M_0 with photochemistry simulations since, as pointed by Moses et al. (1995), the

haze production rate estimated in their analysis is substantially lower (about 5 times) than the predictions from photochemical simulations(Moses et al., 1992, 1995; rom, 1993).

Finally, we can also consider the possibility of temporal and latitudinal variations of the haze production rate as a result of other factors such as a meridional transport of aerosols from regions of upwelling to regions of subsidence. This implies that the timescales for a stratospheric meridional transport of haze particles are smaller than those given for microphysics (or in terms of velocities that the stratospheric meridional winds are faster than the haze settling velocities). The timescale for a haze particle to be transported a distance equal to the radius of Neptune (R) can be estimated using the following expression

$$t = \frac{R}{w} \tag{8}$$

where w is the meridional wind. From Eq. 8 and the timescales shown in Fig. 21, we can compute for each altitude the equivalent wind velocity (V^*) that represents the wind velocity for which the timescale for haze meridional transport equals the microphysics timescale. If the meridional wind velocity is larger than the equivalent wind velocity, then the haze spatial distribution and its temporal evolution are mainly dominated by dynamics. Figure 23 shows the haze microphysics timescales and the equivalent wind velocities as a function of the pressure, and where we observe that if the meridional wind velocities are larger than $\sim$0.03 ms^{-1} then the dynamics is the main factor controlling the haze distribution in the atmosphere and therefore, the cause of the variations in M_0. Estimations from feature tracking indicate that meridional wind velocities may exceed this velocity at some latitudes (Tollefson et al., 2018). However, these estimations are limited to the altitudes of clouds and may not

be representative of a meridional stratospheric circulation. Therefore, to fully study whether the haze spatial distribution and temporal evolution are dominated by dynamics, GCM simulations are required. These simulations will determine the role played by the global circulation in the distribution of of the haze over the planet.

6 Conclusions

We have used a 1-dimensional microphysical model to simulate the haze formation and evolution in Neptune's atmosphere. These simulations were coupled with the NEMESIS radiative-transfer code to model infrared data in the H-band from VLT/SINFONI acquired in 2013. The choice of using observations in the H-band to constrain the haze properties is based on the fact that these observations for the emission-angle ranges analysed are not significantly affected by the imaginary refractive index of haze particles, reducing, therefore, the number of free parameters required to fit the observations. The main goal of combining microphysics and radiative-transfer simulations was to better estimate the haze vertical profiles of size distribution and number density, which are extremely challenging to constrain from radiative-transfer and ground-based observations alone, and to derive the timescales of microphysics. Our simulations show a haze production rate of $M_0 \sim (2.61 \pm 0.18) \times 10^{-14}$ kg m^{-2} s^{-1} and a particle electric charge of q$\sim$8.6$\pm$1.1 electrons per μm radius at latitudes between 5 and 15° S. This haze production rate is of about ten times greater than that derived for Uranus's atmosphere. Our analyses also indicate the presence of a tropospheric cloud with a total optical depth greater than 10 at 1.46 μm (about 250 times greater than the haze optical depth). The cloud

base, which was found near the 2.5-bar level, may indicate only the top of a thicker and deeper cloud as a result of the large retrieved opacity.

The haze opacity derived in this work is about 3.5 times larger than that obtained by Moses et al. (1995) from Voyager-2 observations in 1989. In terms of M_0, we found that this larger opacity indicates a production rate at least two times larger than the one derived from Voyager-2 observations. The analysis of section 5 indicates that the haze microphysics timescales are of about 15 years at the 0.1-bar pressure level. As a consequence, temporal variations in the haze production rate due to seasonal variations in the solar illumination at the top of the atmosphere might affect the haze structure during the time lapsed between Voyager-2 and 2013. Although this seasonal variability may explain the variations of M_0, the elapsed time between these observations represents only a $\sim$1/7 of a Neptunian year with a monthly mean solar insolation that has not changed significantly at the studied latitudes. The different estimations of M_0 may be due to: a) in our analysis we used infrared data to constrain the haze properties, while Moses et al. (1995) analyzed photometric images at 5 different filters in the visible. While high-phase-angle Voyager observations are more sensitive to small haze particles and at altitudes above the 0.1-bar level, the haze constraints derived from VLT spectra in H-band are limited to pressures greater than 0.1 bar. As a result of the different phase angles of the two set of observations, differences in the estimation of M_0 may arise from the use of Mie phase functions as well. b) the transport of haze particles from different regions of the planet. Meridional winds greater than the equivalent wind velocities illustrated in Fig. 23 may result in temporal and latitudinal variations in the haze structure and, hence, in M_0. To further address this point, however, GCM models capable of modelling the transport of haze and the photochemistry are required. These simulations compared or coupled with

haze microphysics will determine how efficient dynamics is in distributing the haze in the atmosphere.

Although the haze production rate estimated in this work is significantly larger than that from Voyager observations, photochemical models point to even larger production rates on Neptune (by a factor of 2.4). Assuming that the photochemical simulations are correct, we found that this discrepancy can be explained if haze particles evaporate before reaching the tropospheric-cloud levels. This scenario would decrease the cumulative haze opacity above the 1-bar level, and thus a larger haze production rate would be required to fit VLT observations. However, to validate this haze vertical structure future microphysical simulations that include the evaporation rates of haze particles are required.

Acknowledgements

The VLT/SINFONI observations were performed at the European Southern Observatory (ESO), Proposal 092.C-0187. Daniel Toledo, Patrick Irwin and Nicholas Teanby acknowledge the support of the UK Science and Technology Facilities Council. Leigh Fletcher was supported by a Royal Society Research Fellowship and European Research Council Consolidator Grant (under the European Union's Horizon 2020 research and innovation programme, grant agreement number 723890) at the University of Leicester. Glenn Orton acknowledges support from the National Aeronautics and Space Administration that were distributed to the Jet Propulsion Laboratory, California Institute of Technology. Telescope data are publicy available in ESO repository (http://archive.eso.org/eso/eso_archive_main.html).

References

Aplin, K., Harrison, R. G., 2016. Determining solar effects in Neptune's atmosphere. Nature communications 7, 11976.

Borysow, A., Borysow, J., Fu, Y., 2000. Semi-empirical model of collision-induced absorption spectra of H2–H2 complexes in the second overtone band of hydrogen at temperatures from 50 to 500 K. Icarus 145 (2), 601–608.

Borysow, A., Frommhold, L., 1987. Collision-induced rototranslational absorption spectra of CH4-CH4 pairs at temperatures from 50 to 300 K. The Astrophysical Journal 318, 940–943.

Borysow, A., Frommhold, L., Moraldi, M., 1989. Collision-induced infrared spectra of H2-He pairs involving 0-1 vibrational transitions and temperatures from 18 to 7000 K. The Astrophysical Journal 336, 495–503.

Cabane, M., Chassefiere, E., Israel, G., 1992. Formation and growth of photochemical aerosols in Titan's atmosphere. Icarus 96 (2), 176–189.

Campargue, A., Wang, L., Mondelain, D., Kassi, S., Bézard, B., Lellouch, E., Coustenis, A., De Bergh, C., Hirtzig, M., Drossart, P., 2012. An empirical line list for methane in the 1.26–1.71 μm region for planetary investigations (T= 80–300 K). Application to Titan. Icarus 219 (1), 110–128.

Fuchs, N., 1964. The Mechanics of Aerosols 1964. Pagamon, New York.

Irwin, P., Fletcher, L. N., Tice, D., Owen, S., Orton, G., Teanby, N., Davis, G., 2016a. Time variability of Neptune's horizontal and vertical cloud structure revealed by VLT/SINFONI and Gemini/NIFS from 2009 to 2013. Icarus 271, 418–437.

Irwin, P., Lellouch, E., De Bergh, C., Courtin, R., Bézard, B., Fletcher, L., Orton, G., Teanby, N., Calcutt, S., Tice, D., et al., 2014. Line-by-line analysis of Neptune's near-IR spectrum observed with Gemini/NIFS and

VLT/CRIRES. Icarus 227, 37–48.

Irwin, P., Teanby, N., Davis, G., Fletcher, L., Orton, G., Tice, D., Hurley, J., Calcutt, S., 2011. Multispectral imaging observations of Neptune's cloud structure with Gemini-North. Icarus 216 (1), 141–158.

Irwin, P., Teanby, N., De Kok, R., Fletcher, L., Howett, C., Tsang, C., Wilson, C., Calcutt, S., Nixon, C., Parrish, P., 2008. The NEMESIS planetary atmosphere radiative transfer and retrieval tool. Journal of Quantitative Spectroscopy and Radiative Transfer 109 (6), 1136–1150.

Irwin, P. G., Toledo, D., Garland, R., Teanby, N. A., Fletcher, L. N., Orton, G. A., Bézard, B., 2018. Detection of hydrogen sulfide above the clouds in Uranus's atmosphere. Nature Astronomy 2 (5), 420.

Irwin, P. G., Toledo, D., Garland, R., Teanby, N. A., Fletcher, L. N., Orton, G. S., Bézard, B., 2019. Probable detection of hydrogen sulphide (H2S) in Neptune's atmosphere. Icarus 321, 550–563.

Irwin, P. G., Wong, M. H., Simon, A. A., Orton, G., Toledo, D., 2017. HST/WFC3 observations of Uranus' 2014 storm clouds and comparison with VLT/SINFONI and IRTF/Spex observations. Icarus 288, 99–119.

Irwin, P. G. J., Fletcher, L. N., Read, P. L., Tice, D., de Pater, I., Orton, G. S., Teanby, N. A., Davis, G. R., 2016b. Spectral analysis of Uranus' 2014 bright storm with VLT/SINFONI. Icarus 264, 72–89.

Karkoschka, E., Tomasko, M., 2009. The haze and methane distributions on Uranus from HST-STIS spectroscopy. Icarus 202 (1), 287–309.

Karkoschka, E., Tomasko, M. G., 2011. The haze and methane distributions on Neptune from HST–STIS spectroscopy. Icarus 211 (1), 780–797.

Lellouch, E., Hartogh, P., Feuchtgruber, H., Vandenbussche, B., De Graauw, T., Moreno, R., Jarchow, C., Cavalié, T., Orton, G., Banaszkiewicz, M., et al., 2010. First results of Herschel-PACS observations of Neptune. As-

tronomy & Astrophysics 518, L152.

Lindal, G. F., 1992. The atmosphere of Neptune-an analysis of radio occultation data acquired with Voyager 2. The Astronomical Journal 103, 967–982.

Lockwood, G., Thompson, D., 2002. Photometric variability of Neptune, 1972–2000. Icarus 156 (1), 37–51.

Moses, J. I., Allen, M., Yung, Y. L., 1992. Hydrocarbon nucleation and aerosol formation in Neptune's atmosphere. Icarus 99 (2), 318–346.

Moses, J. I., Fletcher, L. N., Greathouse, T. K., Orton, G. S., Hue, V., 2018. Seasonal stratospheric photochemistry on Uranus and Neptune. Icarus 307, 124–145.

Moses, J. I., Rages, K., Pollack, J. B., 1995. An analysis of Neptune's stratospheric haze using high-phase-angle Voyager images. Icarus 113 (2), 232–266.

Pollack, J. B., Rages, K., Pope, S. K., Tomasko, M. G., Romani, P. N., Atreya, S. K., 1987. Nature of the stratospheric haze on Uranus: Evidence for condensed hydrocarbons. Journal of Geophysical Research: Space Physics 92 (A13), 15037–15065.

Rannou, P., Hourdin, F., McKay, C., Luz, D., 2004. A coupled dynamics-microphysics model of Titan's atmosphere. Icarus 170 (2), 443–462.

Romani, P. N., Bishop, J., Bézard, B., Atreya, S., 1993. Methane photochemistry on Neptune: Ethane and acetylene mixing ratios and haze production. Icarus 106 (2), 442–463.

Sheik-Bahae, M., 2005. Nonlinear optics basics. Kramers-Kronig relations in nonlinear optics. Encyclopedia of Modern Optics, 234–239.

Smith, B. A., Soderblom, L. A., Banfield, D., Basilevsky, A., Beebe, R., Bollinger, K., Boyce, J., Brahic, A., Briggs, G., Brown, R., et al., 1989. Voyager 2 at Neptune: Imaging science results. Science 246 (4936), 1422–

1449.

Toledo, D., Irwin, P. G., Rannou, P., Teanby, N. A., Simon, A. A., Wong, M. H., Orton, G. S., 2019. Constraints on Uranus's haze structure, formation and transport. Icarus.

Tollefson, J., de Pater, I., Marcus, P. S., Luszcz-Cook, S., Sromovsky, L. A., Fry, P. M., Fletcher, L. N., Wong, M. H., 2018. Vertical wind shear in Neptune's upper atmosphere explained with a modified thermal wind equation. Icarus 311, 317–339.

Toon, O. B., Turco, R., Pollack, J. B., 1980. A physical model of Titan's clouds. Icarus 43 (3), 260–282.

Zheng, C., Borysow, A., 1995. Modeling of collision-induced infrared absorption spectra of H2 pairs in the first overtone band at temperatures from 20 to 500 K. Icarus 113 (1), 84–90.

Table 1

Values of p_{0i} and M_{0i} (see equations 1-2) used in model-1, model-2 and model-3 for the simulation of the haze production region.

	Model-1	Model-2	Model-3
Region-1	p_{01}=0.016bar	p_{01}=0.016bar	p_{01}=0.016bar
Region-2	-	p_{02}=0.008bar	p_{02}=0.009bar
Region-3	-	p_{03}=0.011bar	p_{03}=0.011bar
Region-1	M_{01}=M_0	M_{01}=0.8×M_0	M_{01}=0.81×M_0
Region-2	-	M_{02}=0.1×M_0	M_{02}=0.16×M_0
Region-3	-	M_{03}=0.1×M_0	M_{03}=0.03×M_0

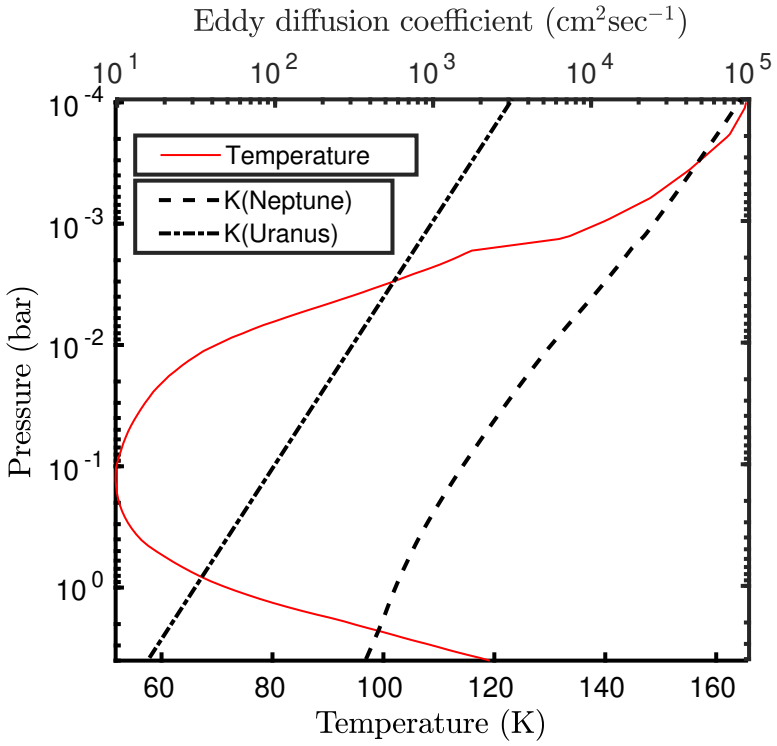

Fig. 1. Variation of temperature and eddy diffusion coefficient with height in Neptune's atmosphere. For comparison purposes, the eddy diffusion coefficient in Uranus's atmosphere is also shown.

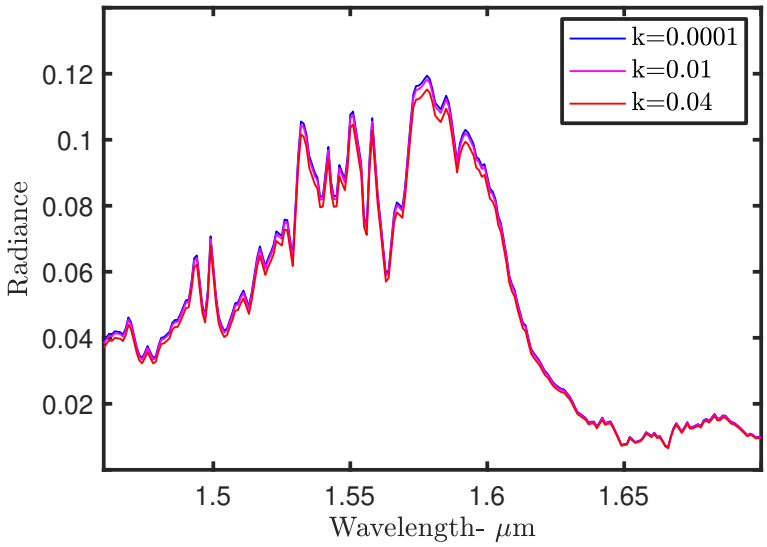

Fig. 2. H-band spectrum (μW cm^{-2} sr^{-1} μm^{-1}) simulated for a haze r$_{eff}$=0.3 μm and different values of the haze imaginary refractive index. The tropospheric cloud properties derived in section 3.3 were used for these simulations.

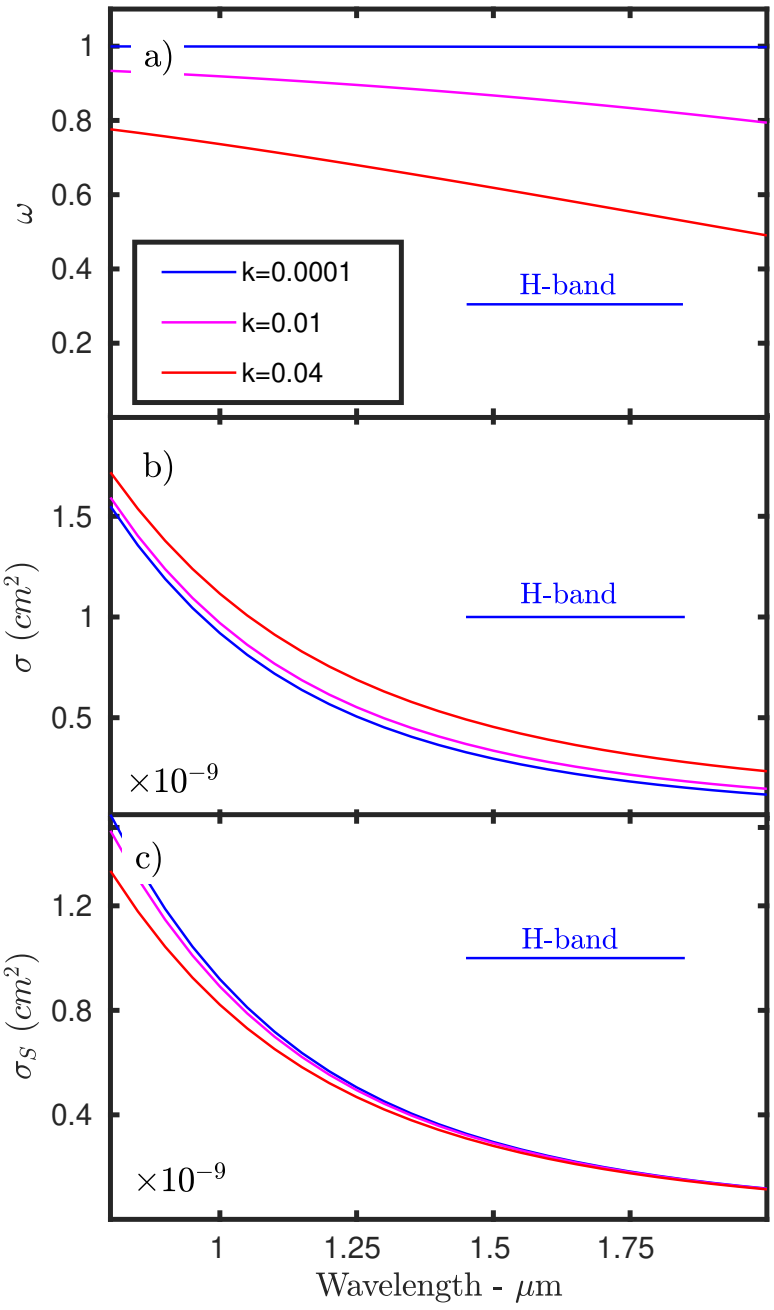

Fig. 3. Spectrum of the single-scattering albedo (panel a), cross section (panel b) and scattering cross-section (panel c) computed with Mie theory for a r_{eff}=0.3 μm and different values of the imaginary refractive index. In all the case the real refractive index was set to 1.4.

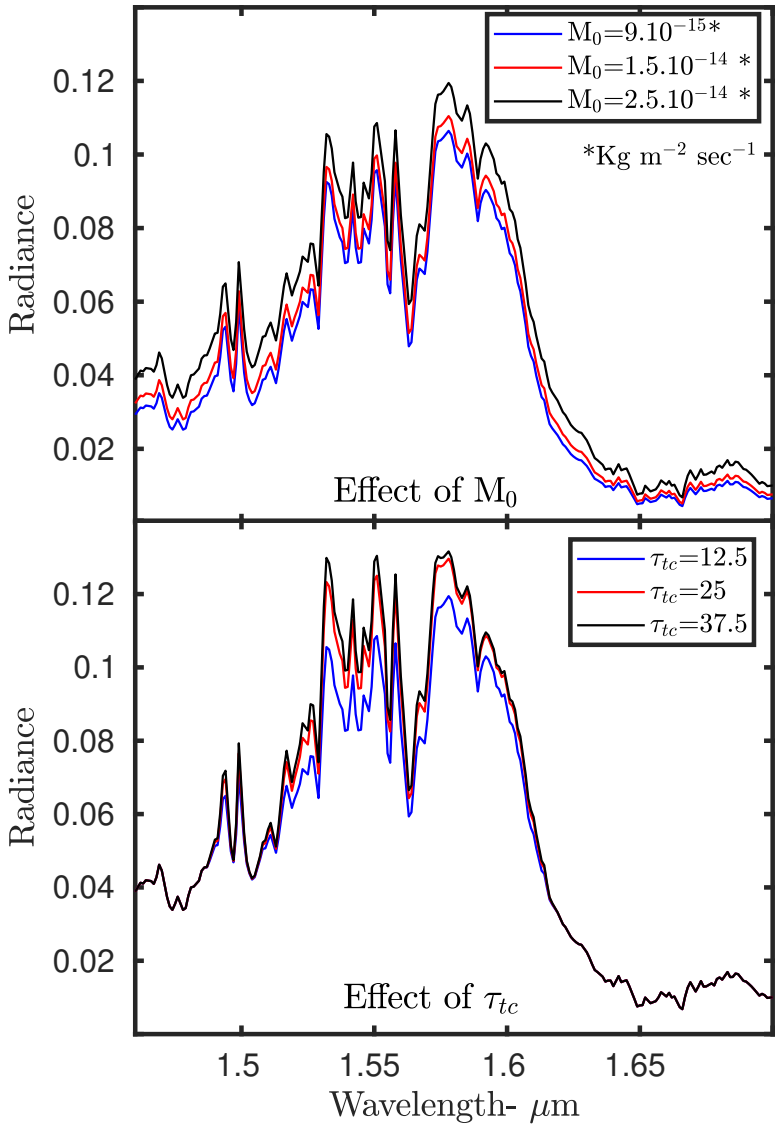

Fig. 4. Variation of the VLT simulated spectrum (μW cm^{-2} sr^{-1} μm^{-1}) with the haze production rate (upper panel) and the tropospheric cloud opacity (lower panel).

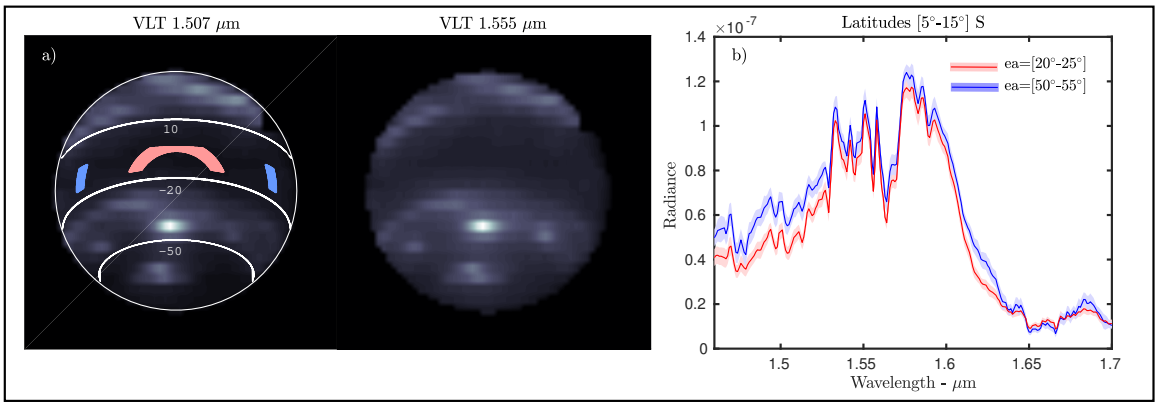

Fig. 5. (a) Very Large Telescope (VLT) images of Neptune at 1.507 and 1.555 μm made in October 2013. The areas highlighted in red and blue indicate pixels at latitudes between 5° and 15° S and with emission angles of between 20 and 25° (red), and of between 50 and 55° (blue). (b) Spectra (μW cm^{-2} sr^{-1} μm^{-1}) obtained from the average of the observations lying in the red area and in the blue area. The shaded errors represent the 1-standard deviation.

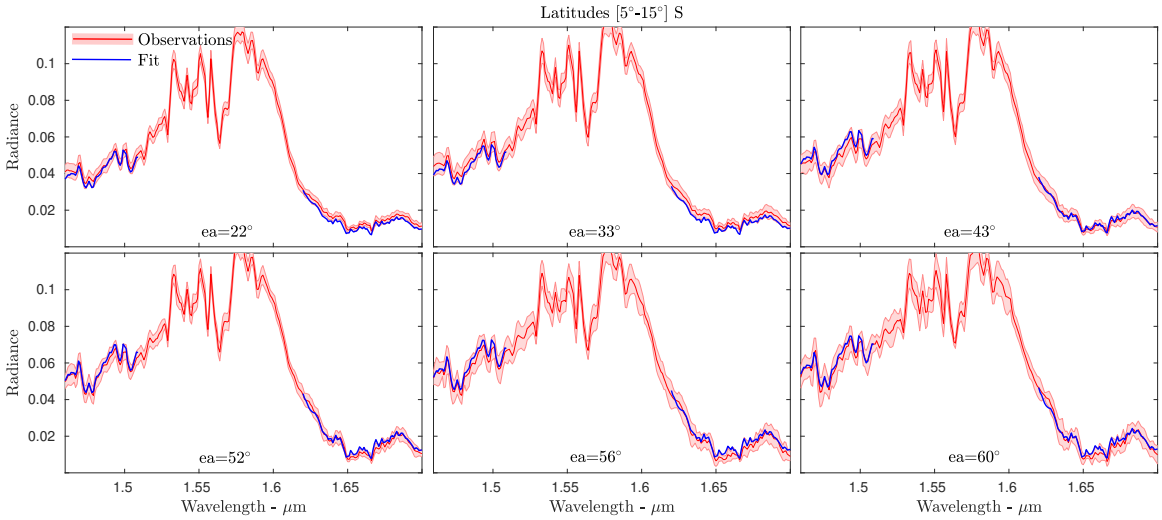

Fig. 6. Comparisons between simulations and observations at latitudes between 5° and 15° S. The thick red solid lines represents VLT spectra computed as in Fig. 5 but for the emission angle (ea) ranges [20°, 25°], [30°, 35°],[40°, 45°], [50°, 54°], [55°, 58°], [59°, 60°]. The blue lines represent the simulations performed for a haze production rate of 2.5×10^{-14} kg m^{-2} s^{-1} and an electric charge of q=10 electrons per μm radius.

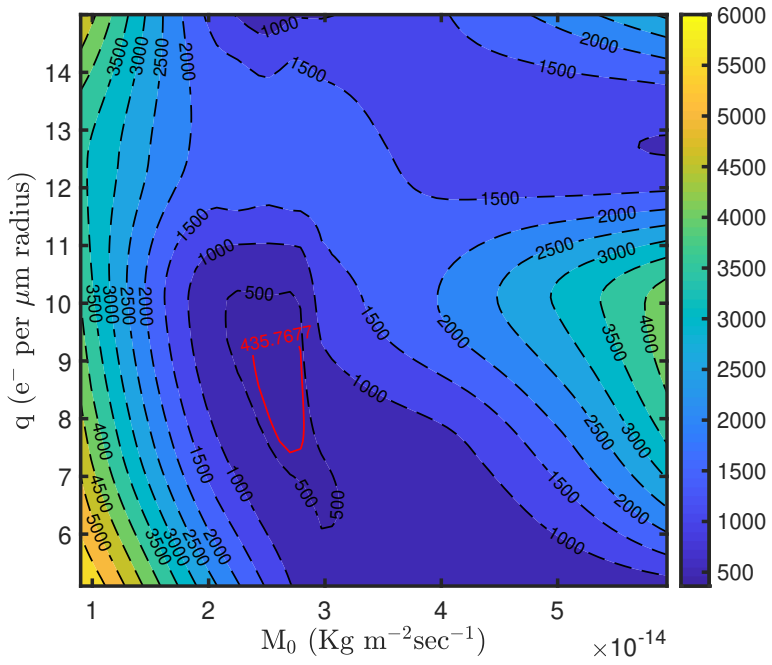

Fig. 7. Contours of χ^2 in the M_0-q parameter space for the spectra given in Fig. 6. The red solid line shows the 3σ significance level.

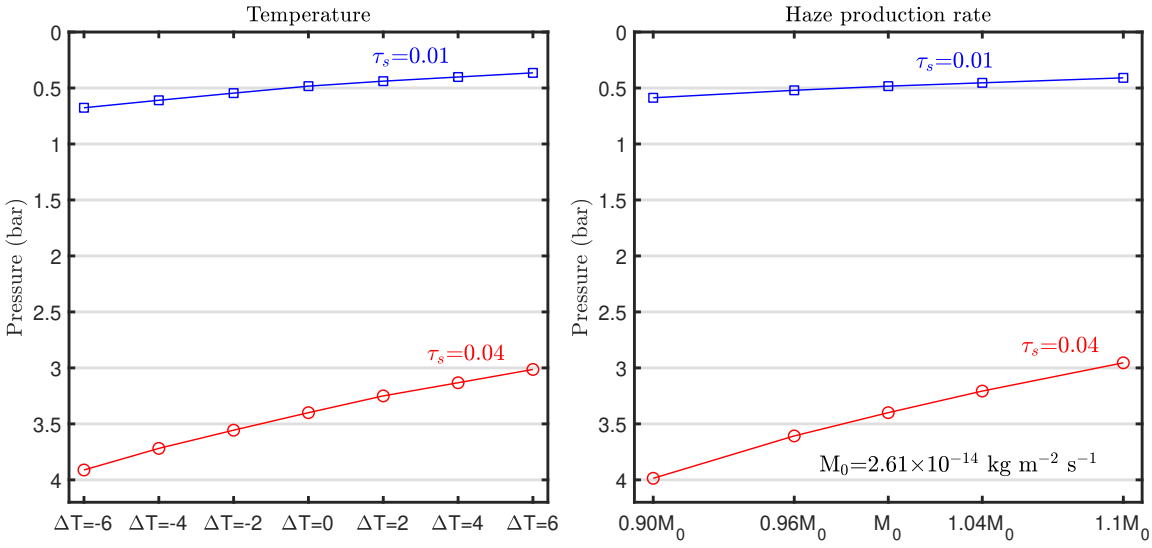

Fig. 8. Pressure level at which the haze cumulative optical depth τ_s is 0.01 (blue line) and 0.04 (red line) for different ΔT (left) and haze production rates M_0 (right).

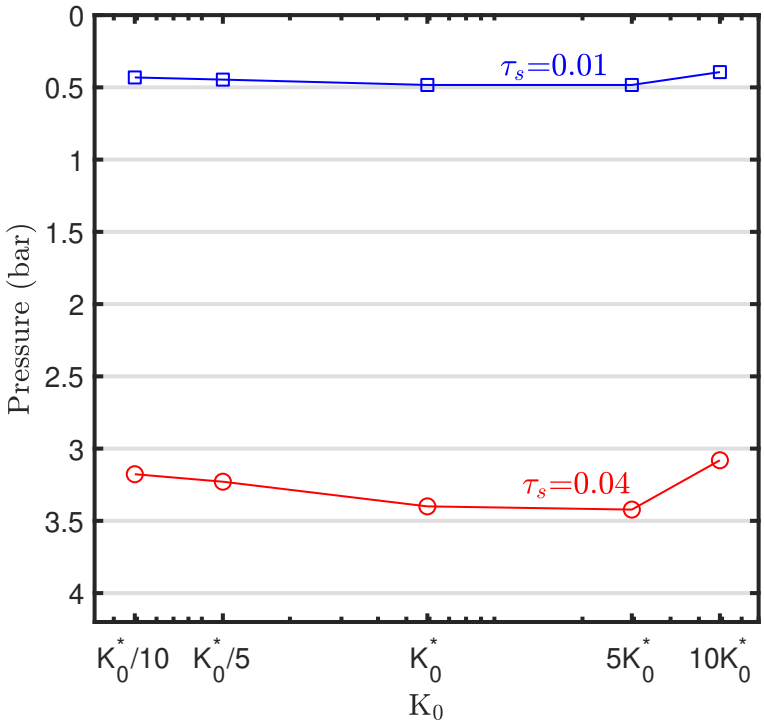

Fig. 9. Pressure level at which the haze cumulative optical depth τ_s is 0.01 (blue line) and 0.04 (red line) for different values of K_0 (see equation 4). K_0^* represents the value used for the profile shown in Fig. 1.

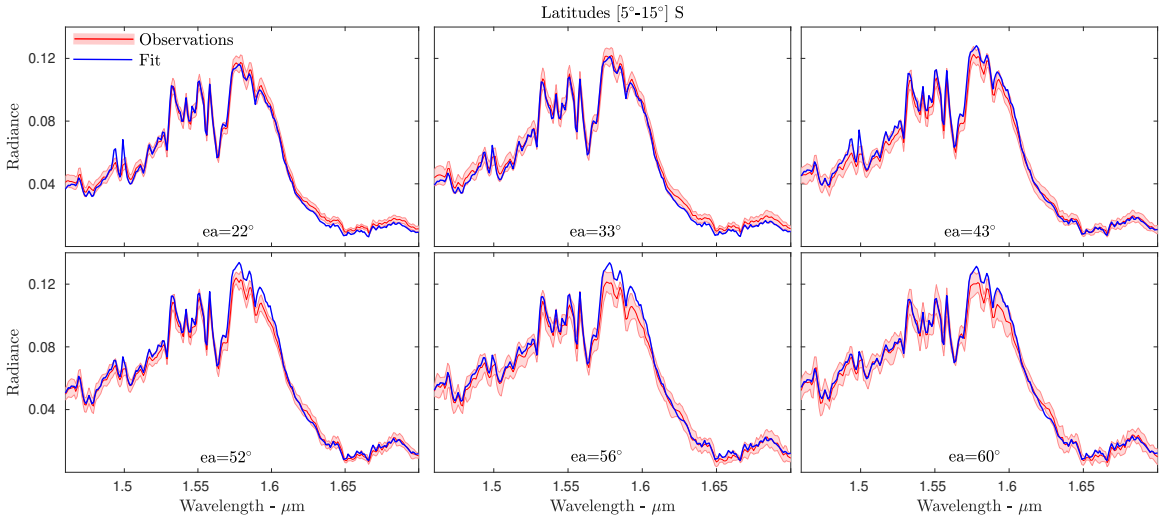

Fig. 10. Comparisons between simulations and observations at latitudes between 5° and 15° S. The thick red solid lines represents VLT spectra illustrated in Fig. 6, and the blue lines are simulations obtained from the optimal solutions of the tropospheric cloud parameters and the haze parameter derived in section 3.3.

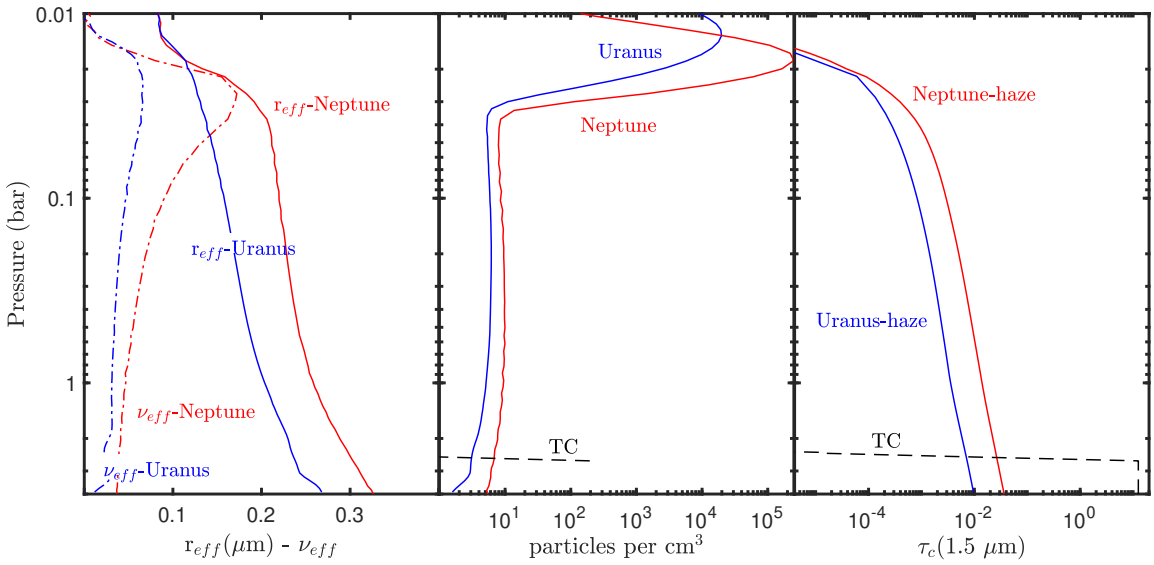

Fig. 11. Aerosol vertical profiles of size distribution (left panel), number density (central panel) and cumulative optical depth (right panel) derived in our analysis. For comparison purposes, the haze profiles in Uranus derived in Toledo et al. (2019) are also shown. The black dashed lines in the central and right panels indicate the number density and opacity of the tropospheric cloud (TC).

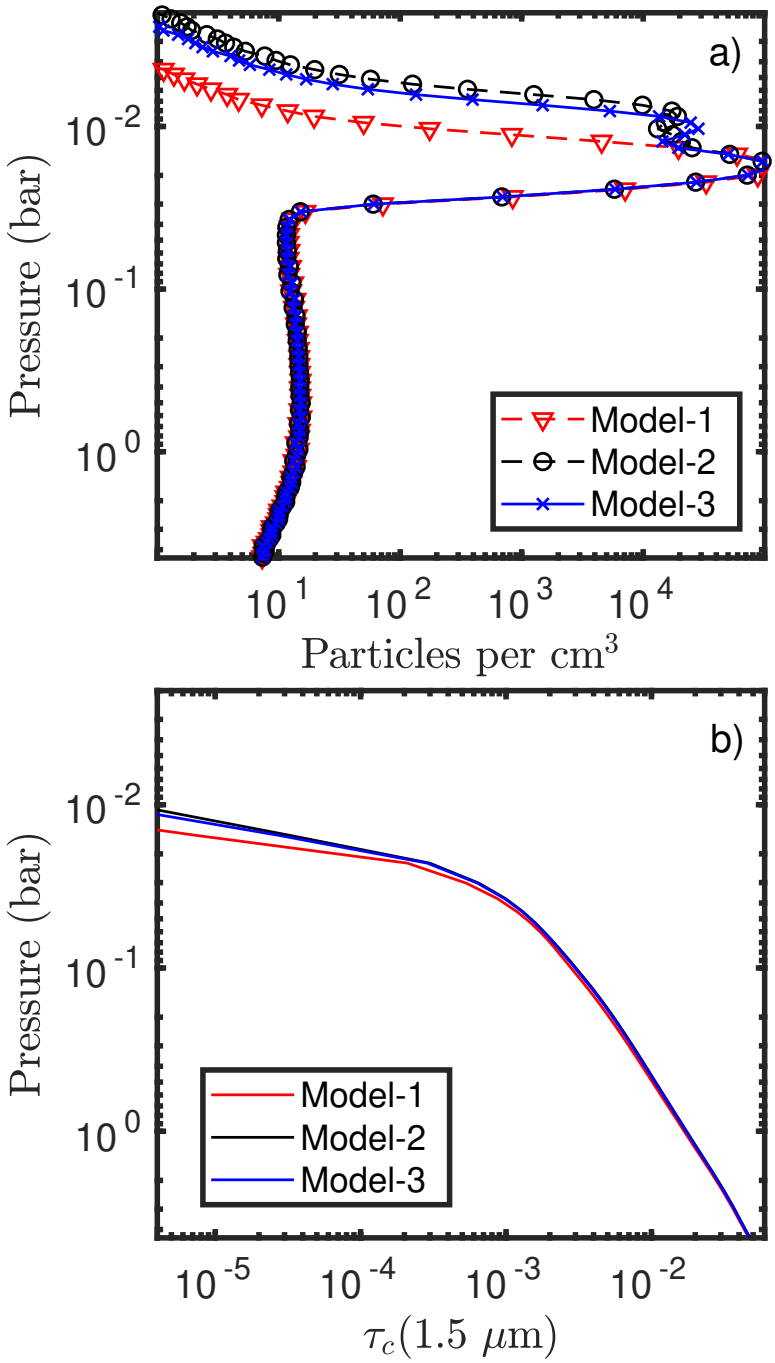

Fig. 12. Haze profiles of number density (upper panel) and cumulative optical depth (lower panel) computed with our haze microphysical model for the haze production models illustrated in Table 6. The optical depth was computed assuming a constant refractive index of n=1.4+0.0001i.

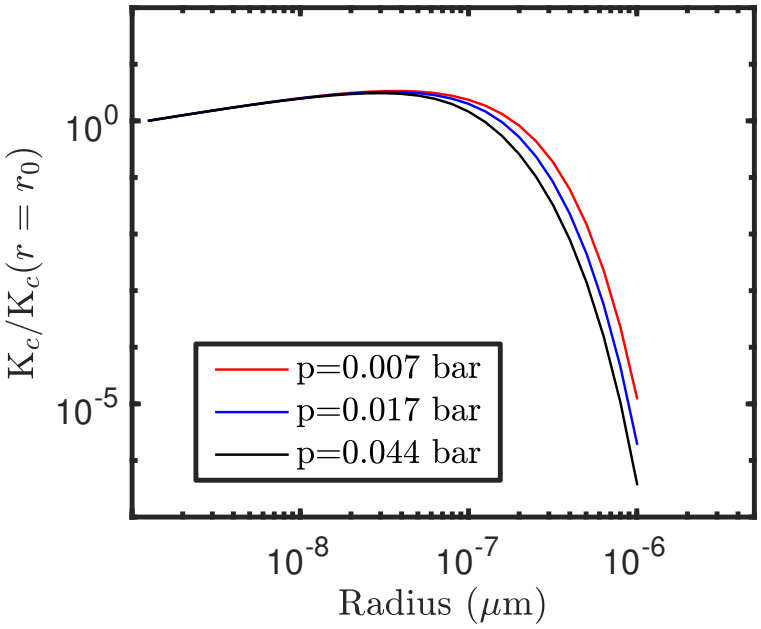

Fig. 13. Variation of the collection kernel K_c with particle radius at 3 different pressure levels of the atmosphere. The values are normalized to the value of K_c for $r=r_0$.

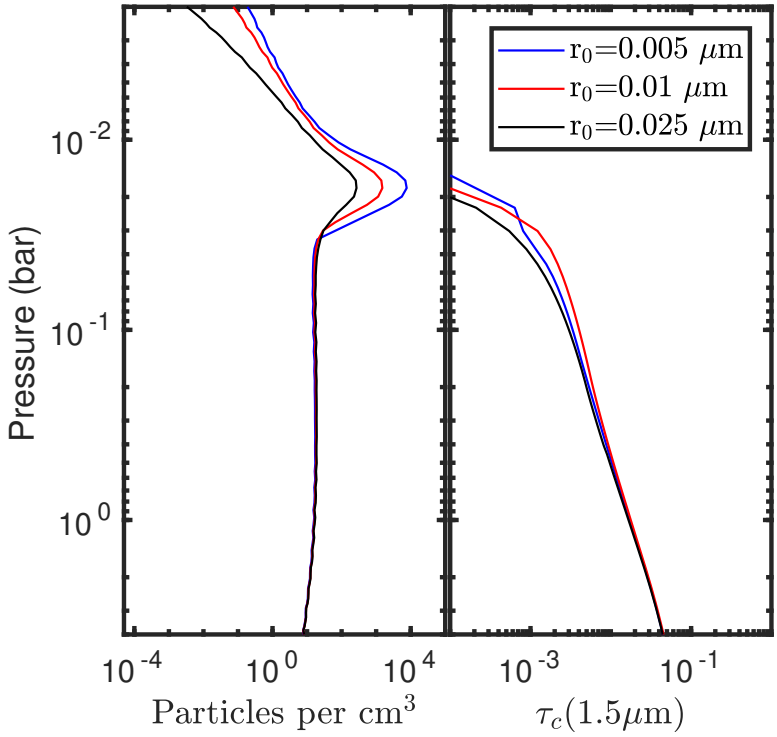

Fig. 14. Haze profiles of number density (left panel) and cumulative optical depth (right panel) computed with our haze microphysical model for different initial model radii r_0 and a haze production rate of 2.5×10^{-14} kg m^{-2} s^{-1}.

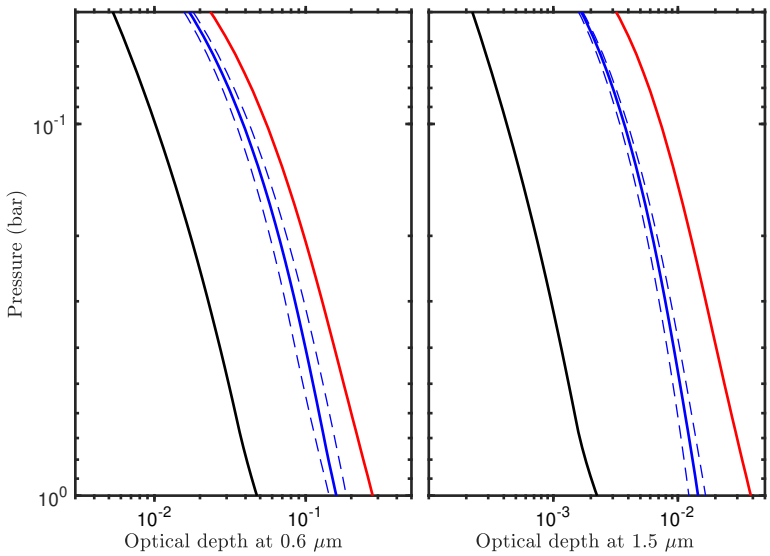

Fig. 15. Cumulative optical depth at 0.6 and 1.5 μm computed for the haze parameters derived in section 3.3 (blue solid lines with errors represented by dashed blue lines) and for M1995 haze parameters (black solid lines). For comparison purposes, the optical depth obtained for a haze production rate of 6×10^{-14} kg m^{-2} s^{-1} is also given (red solid lines).

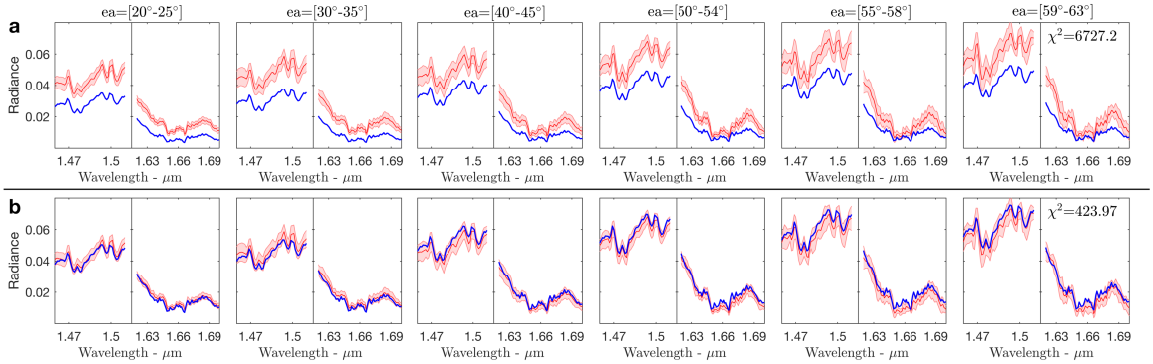

Fig. 16. Comparison between simulations and observations at latitudes between 5° and 15° S. The thick red solid lines represent the VLT spectra illustrated in Fig. 6, and the blue lines are simulations performed for M1995 haze parameters (a) and for the haze optimal solution derived in section 3.3 (b)

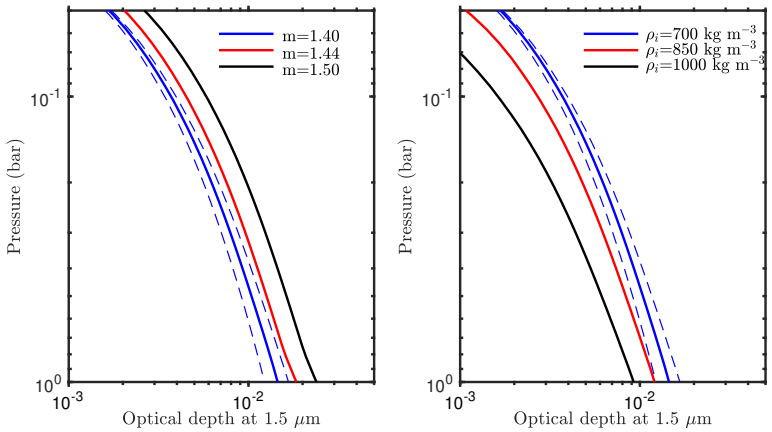

Fig. 17. Variation of the haze optical depth with the real refractive index (left panel) and the density of the haze particles (right panel). In both cases the blue solid line with errors (dashed lines) represents the profile obtained for T2020 parameters.

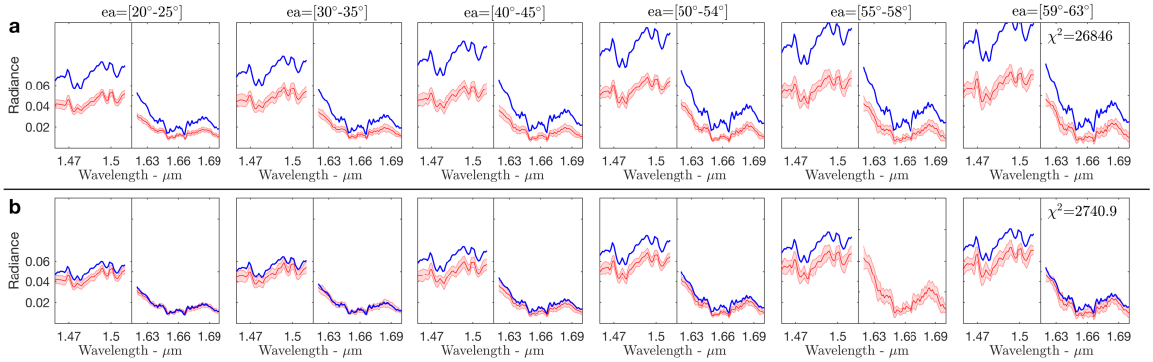

Fig. 18. Comparison between simulations and observations at latitudes between 5° and 15° S. The thick red solid lines represent the VLT spectra illustrated in Fig. 6, and the blue lines are simulations performed for a haze production rate of 6×10^{-14} kg m^{-2} s^{-1} and a density of haze particles ρ_i of 700 kg m^{-3} (a) and 1000 kg m^{-3} (b). In both cases the real refractive index was set to 1.4.

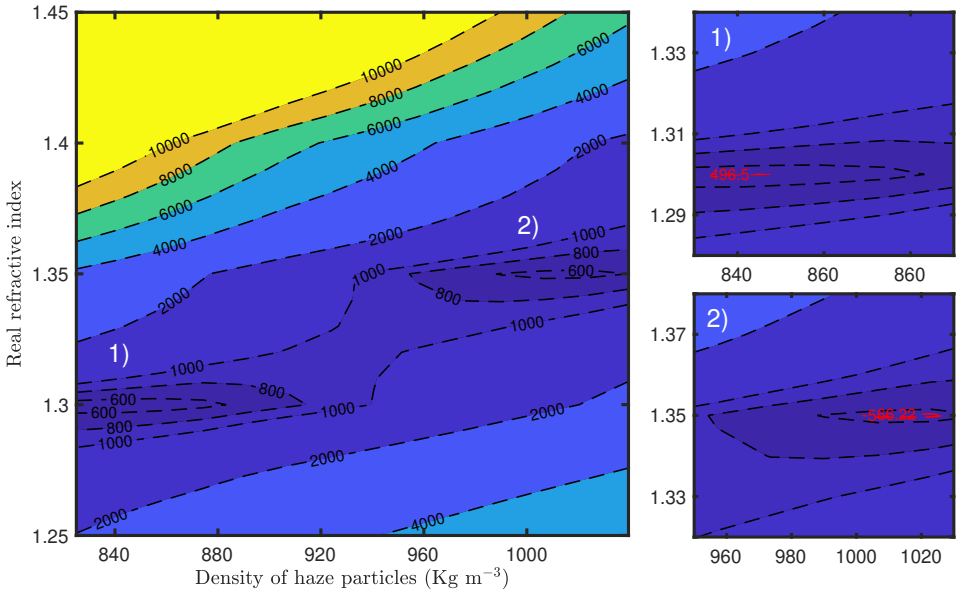

Fig. 19. Contours of χ^2 in the ρ_i-m parameter space for the spectra shown in Fig. 6. For all the simulations the haze production rate was fixed to 6×10^{-14} kg m^{-2} s^{-1}. The red dashed lines show the 3σ significance levels of the two minima.

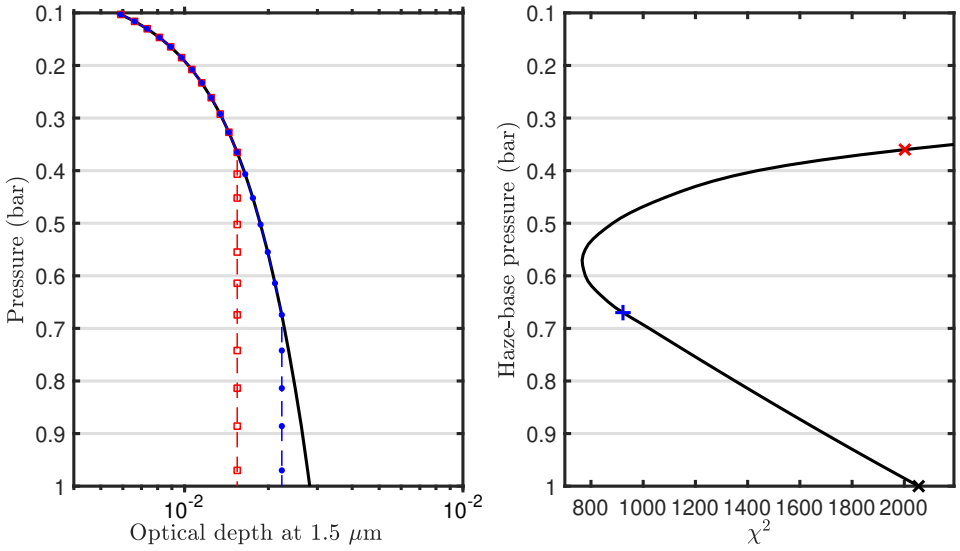

Fig. 20. Left) Cumulative optical depth at 1.5 μm computed for a haze production rate of 6×10^{-14} kg m^{-2} s^{-1} and setting the haze-base pressure at 0.36 bar (red curve), 0.67 bar (blue curve) and 1 bar (black curve). The rest of haze parameters were set to T2020 values. Right) Variation of χ^2 with the haze-base pressure. The haze parameters were set to the values used in Fig. 18a, and the crosses indicate the χ^2 values achieved for the profiles of left panel.

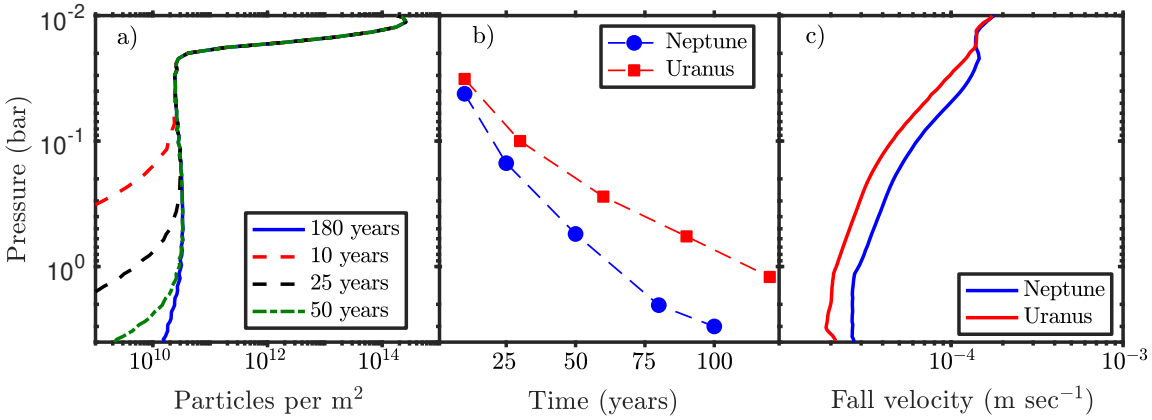

Fig. 21. (a) Haze density profile computed for Neptune's atmosphere with our haze microphysical model for different time scales using a haze production rate of $M_0 2.5\times10^{-14}$ kg m^{-2} s^{-1} and q=10 e$^-$ per μm radius. (b) Variation of haze microphysics timescale with pressure for a haze production of 2.5×10^{-14} (Neptune) and 3×10^{-15} kg m^{-2} s^{-1} (Uranus). (c) Variation of fall velocity with altitude in Neptune and Uranus for the haze particles radius illustrated in left panel of Fig. 11.

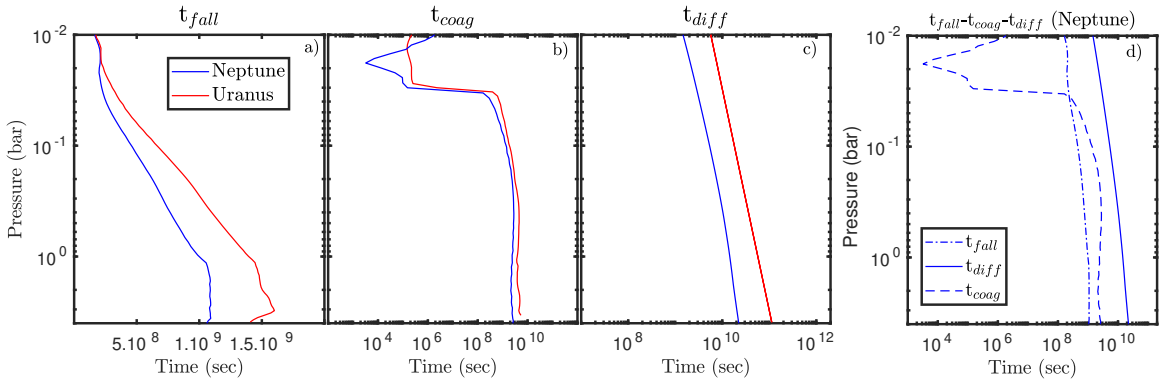

Fig. 22. Comparison of the sedimentation (panel a), particle coagulation (panel b) and eddy diffusion (panel c) timescales in Neptune and Uranus computed for a haze production of 2.5×10^{-14} (Neptune) and 3×10^{-15} kg m^{-2} s^{-1} (Uranus). Panel d shows a comparison between these timescales for Neptune.

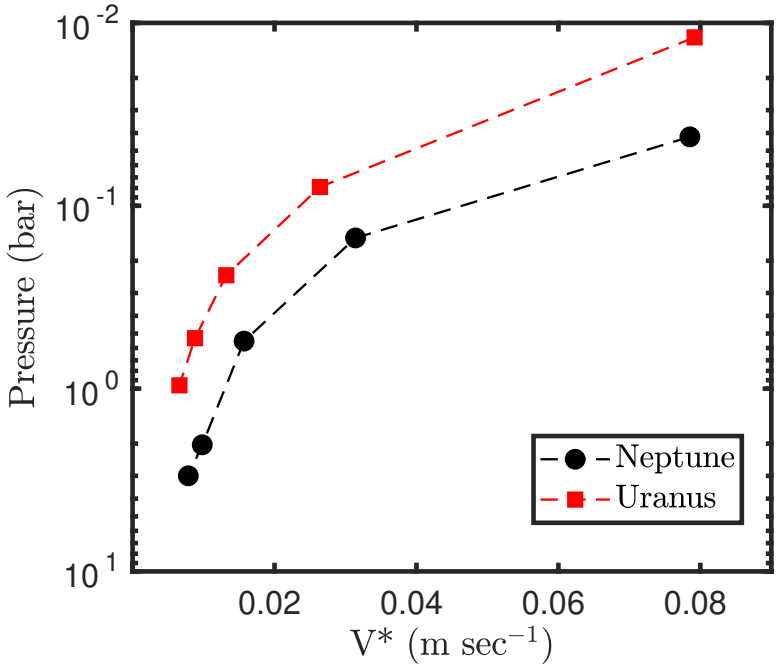

Fig. 23. Variation of the equivalent wind velocity with altitude in Neptune and Uranus computed from the timescales shown in Fig. 21. Note that the equivalent wind velocities in Neptune are greater than in Uranus as a result of its smaller t_M.